Real-space origin of topological band gaps, localization, and reentrant phase transitions in gyroscopic metamaterials

Noah P. Mitchell [1,2,*] Ari M. Turner,[3,†] and William T. M. Irvine [2,4,‡]

[1]*Kavli Institute for Theoretical Physics, University of California Santa Barbara, Santa Barbara, California 93106, USA*
[2]*James Franck Institute and Department of Physics, University of Chicago, 929 E. 57th St., Chicago, Illinois 60637, USA*
[3]*Department of Physics, Technion, Haifa, Israel, 320000*
[4]*Enrico Fermi Institute, University of Chicago, 5640 S. Ellis Ave., Chicago, Illinois 60637, USA*

Lattices of interacting gyroscopes naturally support band gaps and topologically protected wave transport along material boundaries. Recently the authors and their collaborators found that amorphous arrangements of such coupled gyroscopes also support nontrivial topological phases. In contrast to periodic systems, for which there is a comprehensive understanding and predictive framework for band gaps and band topology, the theory of spectral gaps and topology for amorphous materials remains less developed. Here we use experiments, numerics, and analytic tools to address the relationship between local interactions and nontrivial topology. We begin with a derivation of the equations of motion within the framework of symplectic mechanics. We then present a general method for predicting whether a gap exists and for approximating the Chern number using only local features of a network, bypassing the costly diagonalization of the system's dynamical matrix. Finally we study how strong disorder interacts with band topology in gyroscopic metamaterials and find that amorphous gyroscopic Chern insulators exhibit similar critical behavior to periodic lattices. Our experiments and simulations additionally reveal a topological Anderson insulation transition, wherein disorder drives a trivial phase into a topological one.

I. INTRODUCTION

The past decade has witnessed a surge of interest in exploiting concepts from topology as a powerful tool to engineer material behavior [1–4]. In particular, an important realization was that collections of a material's normal modes are not merely independent; instead, phase relationships between modes—quantified, for example, by Berry curvature—can have physical implications. This realization provides a natural framework for linking topological ideas to material systems and distinguishing topologically distinct phases of matter [5–7].

These connections have revealed unique phenomena governed by the topology of the band structure of the material in question. Crucially, the resulting exotic effects, such as the appearance of chiral edge modes, are protected from disorder by their topological origin, meaning that chiral edge modes are insensitive to geometric features of the boundary or inhomogeneity in the material's bulk [8,9]. The design of mechanical metamaterials—engineered structures assembled from composite components—has extended topological protection to elastic structures, enabling us to control and direct phononic excitations robustly without requiring extreme precision in the metamaterial's construction [7,10,11].

At the same time, metamaterials offer an ideal arena for fundamental insights into topological phases. In metamaterials, we observe topological excitations directly at a macroscopic scale, rather than through indirect transport measurements. Tabletop metamaterials furthermore support rapid prototyping and access to the material's individual components. This class of platforms has allowed the direct identification of topological behavior in crystalline systems as diverse as coupled pendula [11], photonic waveguides [12], isostatic frames [13], chains of gears [14], and lattices of acoustic resonators [15]. One other emerging platform of metamaterial systems is composed of interacting gyroscopes suspended from a plate [16–22]. Because networks of gyroscopes break time-reversal symmetry in a geometry-dependent manner, these gyroscopic tabletop metamaterials have provided a simple platform to observe topological phase transitions [17] and switch between multiple topological phases with multiple gaps [18].

This ease of access in turn allows for discovery. For example, constructing amorphous materials using the gyroscopic platform provided a route to discovering that topology arises not just in crystalline materials, but even in amorphous networks [23]. This last example suggests that topological phases should arise in glassy systems composed of randomly arranged inclusions, dopants, or vacancies—a prediction that has since been identified in models of quantum matter [24–29]. Some instances of these topological amorphous phases have been suggested to be distinct phases of matter

---

*Corresponding author: npmitchell@kitp.ucsb.edu
†Corresponding author: turner.ari@ph.technion.ac.il
‡Corresponding author: wtmirvine@uchicago.edu

[25,30] and have been placed into a topological classification scheme for mechanical systems [31].

These recent discoveries place a spotlight on the importance of local, real-space physics in determining topological phenomena. Here we build methods to predict spectral gaps and estimate band topology from local material structure. We begin by revisiting the symmetries underlying gyroscopic metamaterials reported in [16–18,23] from the point of view of symplectic dynamics. This reveals a previously overlooked change in the normalization of states. While this correction does not affect any previously reported results, we find that other aspects of the system do change—including Berry curvature distributions, the sign of real-space topological invariants for negative-frequency bands, and the appropriate form of the projection operator. We then construct a prediction of spectral gaps that does not require diagonalization of the dynamical matrix, estimate topological invariants using only local neighborhoods of a material, and investigate how couplings between local neighborhoods enable long-ranged edge modes. This extends the current understanding of the mesoscopic or quasilocal character of band topology that has emerged based on studies of gyroscopic materials.

Last, we present experimental and numerical measurements of phase transitions driven by disorder and the localization properties of gyroscopic materials' band structures. In contrast to recent studies of critical behavior in amorphous topological insulators [25,32], we find the scaling behavior of critical exponents consistent with the universality class with Cartan label A. In addition, a topological Anderson insulator phase diagram shows reentry into the topological phase with increasing disorder strength, in both experiments and simulations.

II. AN ODD INTERACTION AND ITS SYMPLECTIC DYNAMICS

In this section, we reconsider oscillations of coupled gyroscopes in light of the observation that the dynamics are not Hermitian but *symplectic*. The system is composed of coupled spinning gyroscopes suspended from a plate shown in Fig. 1. When the spinning speed is large, the high-frequency nutation becomes negligible in amplitude. A gyroscope with a hanging orientation vector $\hat{n}$ subjected to forces acting at $\ell\hat{n}$ exhibits motion in the xy plane governed by the action of torques redirecting the angular momentum axis, generating a chiral—or "odd"—equation of motion:

$$\frac{I\omega_0}{\ell}\partial_t x = \ell\frac{\partial U}{\partial y}, \tag{1}$$

$$\frac{I\omega_0}{\ell}\partial_t y = -\ell\frac{\partial U}{\partial x}, \tag{2}$$

where ℓ is distance from the pivot point to the point where forces act, x and y are the in-plane displacements of the same point, U is the potential energy of the gyroscope from pinning forces (like gravity and the springs connecting the gyroscope to its neighbors), ω_0 is the spin frequency, I is the moment of inertia along the spinning axis, and x and y are the displacements from the equilibrium position.

Equations (1) and (2) reflect the unusual behavior of gyroscopes: they respond to an applied force by moving in a
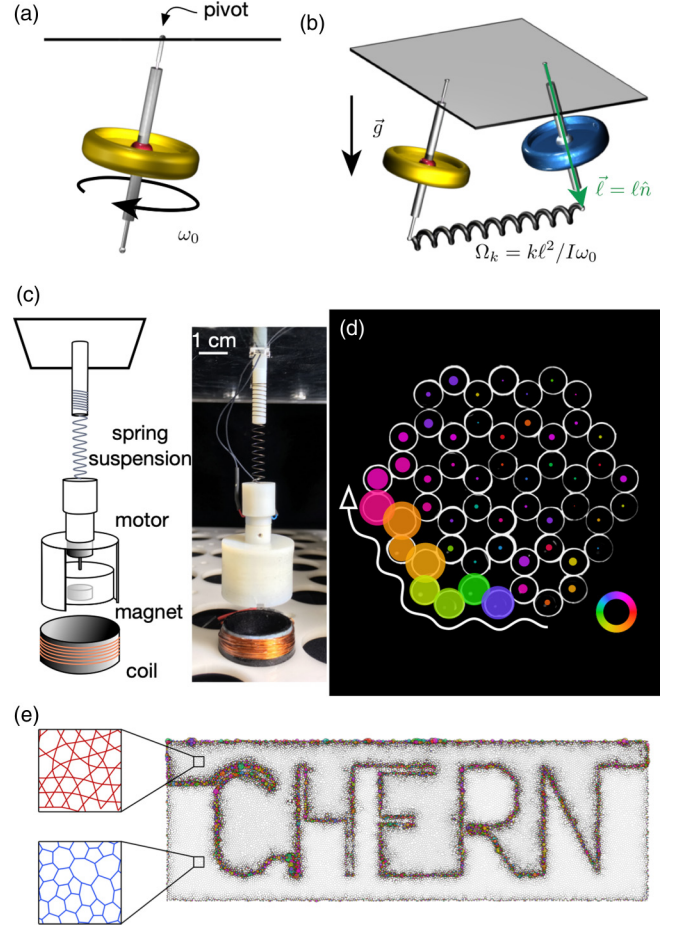

FIG. 1. Gyroscopic metamaterials provide a platform for engineering exotic behavior. (a) Each gyroscope is suspended from a plate and spins rapidly with a speed ω_0. (b) Coupled gyroscopes experience an interaction frequency, Ω_k, and precess under the influence of restoring forces such as gravity. (c) In an experimental realization, externally powered motors spin small masses with magnets embedded at their cores. All gyroscopes spin in the same direction. A weak spring suspends the gyroscope from a plate, enabling low-loss precession, as in Refs. [16,17,23]. In this work, the coil beneath each gyroscope that locally modulates the effective gravitational torque on each gyroscope allows us to introduce disorder and staggered potentials. (d) Chiral waves skim along the boundary when the system is shaken at a frequency in the resulting band gap. Each colored circle represents the measured displacement of a gyroscope in our experimental realization, with the radius proportional to the displacement amplitude and the color denoting the phase (inset shows color wheel). (e) Protected chiral waves persist even if the spatial structure of the underlying network is amorphous, as demonstrated in [23]. Here a simulated amorphous network of gyroscopes consists of a kagome-like structure above and a Voronoi-like structure below a boundary shaped into the letters "CHERN." The upper and lower regions differ in their topological phase, so that an extended wave packet travels along the boundary between the regions.

direction transverse to that force. Building a material out of coupled gyroscopes translates this unusual response into new collective material excitations that are profoundly different
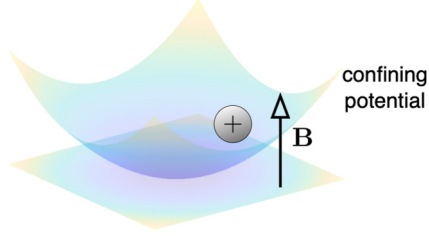
FIG. 2. A charged particle in a magnetic field provides a simple setting in which to understand symplectic dynamics. A particle of positive unit charge moves in a confining potential (blue gradient) and experiences cyclotron orbits due to an out-of-plane magnetic field of strength B.

from those of inertial materials, where we are accustomed to having displacements follow the direction of forces.

In conventional elastic materials, waves emerge from the conversion of potential energy into kinetic energy and back again. As energy sloshes back and forth between two forms, disturbances propagate through the material. For interacting gyroscopes, however, inertia is dominated by the rapid spin of each gyroscope, rendering the kinetic energy of the gyroscopes' center of mass motion irrelevant. Instead, the independent degrees of freedom are the orthogonal gyroscope displacements x and y, and the resulting energy oscillation is an oscillation of potential energy between these two spatial degrees of freedom, which are coupled to one another because of the transverse response of gyroscopes to applied forces. These dynamics are analogous to those of Tkachenko waves in vortex crystals [33].

The relationship between motion in these two directions forms a symplectic structure. By defining $q = \sqrt{I\omega_0}\,x/\ell$ and $p = \sqrt{I\omega_0}\,y/\ell$, we see that Eq. (1) and Eq. (2) are the same as Hamilton's equations:

$$\partial_t q = \frac{\partial U}{\partial p}, \quad \partial_t p = -\frac{\partial U}{\partial q}, \tag{3}$$

which provides symplectic structure to the dynamics.

A. Symplectic structure of cyclotron orbits

To gain some insight into the practical consequences of these conservative transverse dynamics, it is helpful to examine a simple related system, a charged particle in a magnetic field confined by an external potential, as sketched in Fig. 2. This simple example highlights subtleties in this category of problems with time-reversal-broken dynamics.

We take the energy to be given by

$$H = \frac{1}{2m}\left(\vec{p} - \frac{q\vec{A}}{c}\right)^2 + \frac{k}{2}(x^2 + y^2), \tag{4}$$

where we adopt the gauge such that $\vec{A} = Bx\hat{y}$ for the vector potential $\vec{A}$ so that $\vec{B} = B\hat{z} = \vec{\nabla} \times \vec{A}$ and $\vec{p}$ is the canonical momentum. In order to fully describe the normal modes of the particle's motion, both real-space coordinates (x, y) and the conjugate momenta $(p_x = m\partial_t x, \ p_y = m\partial_t y + qBx/c)$ must

be included. Hamilton's equations [Eq. (3)] become

$$\partial_t \begin{pmatrix} x \\ y \\ p_x \\ p_y \end{pmatrix} = \begin{pmatrix} 0 & 0 & \frac{1}{m} & 0 \\ -\frac{qB}{mc} & 0 & 0 & \frac{1}{m} \\ -\frac{q^2B^2}{mc^2} - k & 0 & 0 & \frac{qB}{mc} \\ 0 & -k & 0 & 0 \end{pmatrix} \begin{pmatrix} x \\ y \\ p_x \\ p_y \end{pmatrix}. \tag{5}$$

This is simply a recasting of Hamilton's equations seen before in Eq. (3). Similarly to a quantum mechanical Hamiltonian, the dynamical matrix is a linear operator governing the evolution of the system, but the matrix here is not Hermitian. Instead, it is symplectic, as we will see. The four eigenmodes of the dynamical matrix trace out elliptical orbits, taking the form of

$$e_\pm = \frac{1}{\sqrt{2\omega_\pm\left(m\alpha_\pm^2 + \frac{1}{k}\right)}}\left(\alpha_\pm, \quad \frac{-i\omega_\pm}{k}, \quad im\alpha_\pm\omega_\pm, \quad 1\right) \tag{6}$$

and their complex conjugates, $\overline{e}_+$ and $\overline{e}_-$, where the frequencies of the orbits are $\pm\omega_+$ and $\pm\omega_-$. Above,

$$\alpha_\pm = \frac{c}{qBk}\left(k - m\omega_\pm^2\right), \tag{7}$$

and the eigenmode frequencies are

$$\omega_\pm = \sqrt{\frac{k}{m} + \frac{q^2B^2}{2c^2m^2}\left(1 \pm \sqrt{\frac{4c^2km}{q^2B^2} + 1}\right)}. \tag{8}$$

These eigenmodes, which correspond physically to cyclotron orbits of the particle precessing in the magnetic field, are orthogonal under the symplectic form, defined for any two modes, represented by four-component vectors ψ_α and ψ_β, as

$$\langle \psi_\alpha | \cdot^\perp | \psi_\beta \rangle = i \sum_{j \in \{1,2\}} \overline{x_{\alpha,j}}\, p_{\beta,j} - \overline{p_{\alpha,j}}\, x_{\beta,j}, \tag{9}$$

where $\vec{x} = (x, y)$ and $\vec{p} = (p_x, p_y)$ and j runs over the two spatial dimensions.

This highlights a difference between parity-breaking systems and more common inertial systems that do not break parity. In the latter case, there is a direct proportionality between momentum and velocity. For an eigenmode in an inertial system, the momentum is then simply proportional to the position offset by a phase ($p_j = -im_j\omega x_j$). This simplifies the dynamical matrix considerably to produce eigenvectors that are orthogonal under both the symplectic form and the familiar Euclidean norm defined as $\sum_j m_j x_{\alpha,j} \overline{x_{\beta,j}}$. This feature persists in systems of many coupled inertial objects. In contrast, rotational coupling between motion in x and y prevent the eigenvectors from being orthogonal under the Euclidean inner product. However, under the symplectic form, the eigenmodes *are* orthogonal for any value of magnetic field B according to

$$\langle \psi_\alpha | \cdot^\perp | \psi_\beta \rangle = \delta_{\alpha\beta}\, \text{sgn}(\omega_\alpha). \tag{10}$$

In systems with chiral coupling between positions and momenta, the only appropriate inner product is given by Eq. (9), and this norm relates the time-averaged energy of a mode, $\langle U \rangle$, to the oscillation frequency, ω. This relationship

is given by

$$\omega_\alpha = \frac{\langle U \rangle}{\langle \psi_\alpha | \cdot^\perp | \psi_\alpha \rangle}, \tag{11}$$

which holds only when $\langle \psi_\alpha | \cdot^\perp | \psi_\alpha \rangle$ is the symplectic form of the eigenmode given in Eq. (9). This simple relationship allows one to estimate oscillation frequencies by having an intuitive picture of energies involved in a mechanical deformation.

The consequences of symplecticity extend beyond a redefinition of the inner product: a symmetry between eigenvectors at positive and negative frequencies appears. Each mode appears twice, with one eigenvector representation at frequency ω and a second, redundant eigenvector with frequency $-\omega$ and conjugated position and momentum, but each pair represents the same physical cyclotron orbit. This redundancy in the system foreshadows the emergence of "particle-hole" symmetry in networks of gyroscopes.

B. Coupled gyroscopes yield coupled polarizations

Gyroscopic metamaterials similarly break parity, supporting waves that transfer energy between displacements in the two orthogonal spatial dimensions. We consider the motion of the gyroscopes about their hanging rest configuration. For small displacements (x, y) of the centers of mass, the equation of motion for a gyroscope takes the form

$$\partial_t \begin{pmatrix} x_i \\ y_i \end{pmatrix} \approx \Omega_p \begin{pmatrix} y_i \\ -x_i \end{pmatrix} + \frac{\ell^2}{I\omega_0} \sum_{j=1}^{N} \begin{pmatrix} -F_{ij,y} \\ F_{ij,x} \end{pmatrix}, \tag{12}$$

where Ω_p is the pinning frequency due to gravity and other site-specific restoring potentials such as a magnetic field generated by coils placed beneath each gyroscope [see Figs. 1(b)–1(e) and [16]] and the sum is taken over all N neighbors connected to site i. It is useful to write the displacement of the pth gyroscope as $\psi_p \equiv x_p + i y_p$. In an eigenmode, the gyroscope tip then moves along an ellipse represented by a superposition of clockwise and counterclockwise circular motions:

$$\psi_p = \psi_p^R e^{-i\omega t} + \overline{\psi_p^L} e^{i\omega t}, \tag{13}$$

where $\overline{\psi_p^L}$ is the complex conjugate of ψ_p^L. The coordinates (ψ^R, ψ^L) then act as a useful decomposition for describing eigenmodes. If the frequency of oscillation ω is positive, the first term encodes clockwise motion, while the second encodes counterclockwise motion.

How do these dynamics play out in the simplest scenario of two interacting gyroscopes? One possible motion is uniform precession at a frequency Ω_p, which does not stretch or
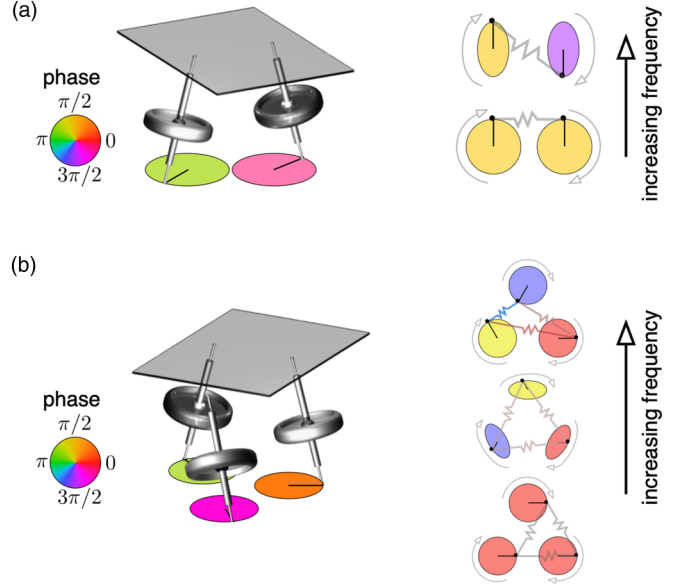

FIG. 3. Interacting gyroscopes highlight the interplay between clockwise and counterclockwise polarizations in elliptical eigenmodes. Eigenmode displacements are represented by ellipses traced out by the gyro tips, each colored by its phase in the ellipse at a snapshot in time. (a) Two interacting gyroscopes support an in-phase circular motion "ground state" ($\omega = \Omega_p$) and out-of-phase elliptical motion "excited state" ($\omega > \Omega_p$). (b) Three interacting gyroscopes generate two excited states in addition to an in-phase circular motion "ground state" ($\omega = \Omega_p$). One has elliptical motion with relative phases staggered by $2\pi/3$, while the highest frequency motion is again circular, with relative phases staggered by $-2\pi/3$. In this figure, we let $\Omega_k = \Omega_p$.

compress the bond connecting the two gyros, shown in the lower mode of Fig. 3(a). This motion is entirely in-phase. The other possible motion is out-of-phase, which does stretch and compress the bond and results in a higher frequency. This out-of-phase motion is elliptical, not circular, as shown in the upper mode of Fig. 3(a). Elliptical traces reflect a superposition of both clockwise and counterclockwise polarizations, foreshadowing that the interaction between polarizations in the dynamical matrix will play a central role in understanding gyroscopic metamaterials. As in the case of a charged particle in a magnetic field, here each of these modes is represented twice—with one eigenstate of frequency ω dominated by ψ^R and one of frequency $-\omega$ dominated by ψ^L. Physically, both ψ^R at positive frequency and ψ^L at negative frequency represent the same clockwise motion according to Eq. (13).

By casting the equations of motion in terms of (ψ^R, ψ^L) as

$$i\partial_t \begin{pmatrix} \psi_p^R \\ \psi_p^L \end{pmatrix} = \Omega_p \begin{pmatrix} \psi_p^R \\ -\psi_p^L \end{pmatrix} + \frac{\Omega_k}{2} \sum_{q \in \mathrm{N}(p)} \begin{pmatrix} \psi_p^R - \psi_q^R + e^{i2\theta_{pq}}(\psi_p^L - \psi_q^L) \\ -\psi_p^L + \psi_q^L - e^{-i2\theta_{pq}}(\psi_p^R - \psi_q^R) \end{pmatrix}, \tag{14}$$

where $\Omega_k = k\ell^2/(I\omega_0)$ is the characteristic spring frequency, θ_{pq} is the bond angle between gyroscopes p and q fixed by network geometry, and the sum over q is over all of p's coupled

neighbors, we see that clockwise and counterclockwise polarizations are coupled through the geometry of bonds between gyroscopes. Here k is the spring constant, ℓ is the length of the

pendulum from the pivot to the point of applied forcing, I is the moment of inertia along the spinning axis, and ω_0 is the angular spinning frequency about the long axis of the gyroscope.

Now that we have gained intuition from the two-gyroscope case, we can formulate the many-gyroscope case as an eigenvalue problem. Equation (14) defines the entries for a system's dynamical matrix, D, such that

$$i\partial_t \vec{\psi} = D\vec{\psi}, \qquad (15)$$

where the components of $\vec{\psi} = (\psi^R, \psi^L)$ encode the displacements of the gyroscopes. The matrix elements D_{ij} describe the response of gyroscope i to displacements of gyroscope j. Note that here D maps displacements in the complex plane to velocities, in contrast to the dynamical matrix of inertial systems [10,22], and both the real and imaginary components are physical observables.

C. Symplecticity affects eigenmodes

The dynamical matrix is not Hermitian. However, due to the symplectic symmetry of our dynamical matrix, all eigenvalues of **D** are nonetheless real. The symplectic symmetry of our dynamical matrix can be stated as

$$D = QD^\dagger Q, \qquad (16)$$

with

$$Q = \begin{pmatrix} \mathbb{I}_n & 0 \\ 0 & -\mathbb{I}_n \end{pmatrix}. \qquad (17)$$

Just as the real-valued frequencies of the charged particle in a magnetic field come in positive and negative pairs, so too the frequencies of gyroscopic motion arise in positive and negative pairs. These two copies of the system's dynamical response are related by a particle-hole symmetry: each eigenmode has two redundant descriptions with frequencies $\pm\omega$ related by $\psi^R \leftrightarrow \overline{\psi^L}$, which exchanges the two terms in Eq. (13). This is analogous to particle-hole symmetry in electronic systems, wherein the behavior of an electron's excited state above the Fermi level is tied to the behavior of a electron "hole" left behind below the Fermi level. In later sections, we find that the symplectic form must be used in the proper definition of Berry curvature and projector operator elements to build real-space descriptions of band topology.

D. Time-reversal symmetry breaking

An interesting transformation to consider is $\psi \to \bar{\psi}$ and $t \to -t$. This transformation is the same as the time-reversal symmetry (TRS) transformation of the Schrödinger equation, which resembles Eq. (14). The conjugation operation $\psi \to \overline{\psi}$, however, has a different interpretation. Here it corresponds to reflecting the displacements $y \to -y$ of each gyroscope about its pivot point. A single gyroscope clearly respects this symmetry, in contrast to a charged particle in a magnetic field; spinning alone does not break this form of TRS.

Interestingly, a system of two interacting gyroscopes also respects TRS. If the bond connecting the two gyroscopes is aligned with the x axis, this follows trivially from the fact that $\theta_{pq} = 0$ or π. Even if the angle θ_{pq} is nonzero, we can globally rotate the system without penalty. Therefore, after
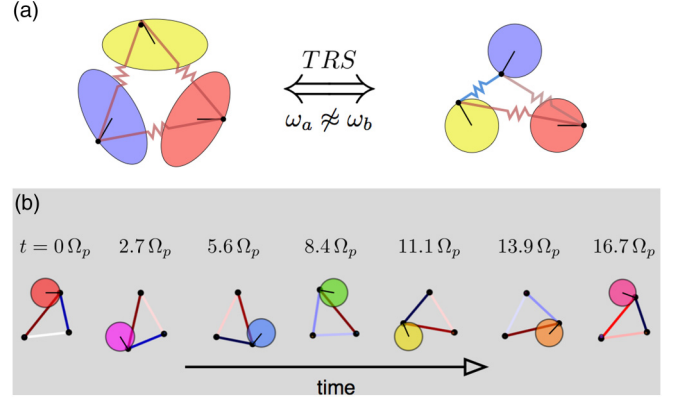

FIG. 4. A triad of gyroscopes provides intuition for the effects of time-reversal symmetry breaking. (a) Time-reversal operation, given by $\psi \to \bar{\psi}$ and $t \to -t$, transforms the instantaneous displacements (black bars) of one eigenmode into another for the gyroscopic triad. Here the instantaneous displacements differ between the two pictured eigenmodes only by $y \to -y$. Since eigenmodes $\vec{\psi}_{\omega_a}$ (left) and $\vec{\psi}_{\omega_p}$ (right) have different frequencies, and given that the time-reversal operator conjugates these displacements, we see that time-reversal symmetry is broken. (b) Simulating the dynamics of the triad reveals strong signatures of chirality from time-reversal symmetry breaking. Because of the phase interference between the different eigenmodes, the displacement generally propagates counterclockwise between the three gyroscopes. For special values of Ω_k/Ω_p, the oscillation is periodically localized to one site at regular intervals, and the site of localized excitation advances in a chiral fashion, here shown for $\Omega_k/\Omega_p = 0.4$. We note that the excitation is not fully localized at times between the snapshots shown.

this coordinate change, the factor $e^{i2\theta_{pq}}$ is purely real, and there is no phase associated with the coupling between polarizations ψ^R and ψ^L.

Introducing a third gyroscope, however, allows time-reversal symmetry to be broken. Now no global rotation of the system will result in bond angles θ_{pq} such that all factors $e^{i2\theta_{pq}}$ are real. The simplest example in which one can observe the role of TRS breaking is the equilateral triad of coupled gyroscopes shown in Fig. 3(b). For this triad, three distinct eigenmodes arise: one uniform in-phase precession with no spring stretching, and two "excited state" motions $\vec{e}_a$ and $\vec{e}_b$. In the particular case of the equilateral triad, neighboring gyroscopes differ in phases by $2\pi/3$ either clockwise (for $\vec{e}_a$) or counterclockwise (for $\vec{e}_b$) around the triangle. The action of the time-reversal operation mixes eigenstates. This can be seen intuitively by examination of the excited states shown in Fig. 4(a). In particular, the time-reversal operation, given by $\psi \to \bar{\psi}$ and $t \to -t$, mixes $\vec{e}_a$ and $\vec{e}_b$, which have different frequencies. In this scenario, we find that TRS breaking is manifest by the difference in frequency of the two eigenmodes that are mixed by the time-reversal operation. More generally, for systems of more than two gyroscopes, time-reversal transforms a given configuration into a linear superposition of modes with different frequencies unless there are additional symmetries that guarantee the bond energy is preserved: time-reversal is not typically a symmetry of the dynamical equations [18].

The lack of TRS in the triad is manifest in the differing frequencies of these eigenmodes. Together with the fact that

the two excited states have differing relative phases between gyroscopes ($\pm 2\pi/3$ rad), the frequency difference between these modes leads to beating patterns with a chiral flow of energy. As shown in Fig. 4(b), displacing a single gyroscope leads to large amplitude excitation that sloshes from one gyroscope to another in a chiral fashion over time. This resulting chiral conductance of energy foreshadows the emergence of chiral edge waves.

Now that we have gained intuition for the role of TRS breaking from the three-gyroscope case, we can see the effects of TRS breaking in the dynamical matrix itself. We can envision excitation of gyroscopes "hopping" from site to site with couplings given directly by the elements of the dynamical matrix **D** in Eq. (15). In fact, we see directly from Eq. (14) that the coupling of clockwise precession and counterclockwise precession depends explicitly on the geometry with *complex* couplings, whereas gyroscopic motion with the same polarization at different sites—ψ_i^R and ψ_j^R, for example—have purely real couplings.

E. Connection to tight-binding models: The limit of weak interactions

If we consider the dynamics when interactions between gyroscopes are weak compared to the pinning forces restoring a gryoscope toward its hanging position, the effects of counterclockwise motion act as a perturbation on the dominant clockwise precession. Figure 5 highlights how the two-gyro and three-gyro cases explored thus far vary as the interaction strength is tuned. Modes that mix polarizations become increasingly elliptical as the coupling strength grows. For weak interactions ($\Omega_k/\Omega_p \ll 1$), gyroscopic networks' eigenmodes become nearly circular, which highlights the perturbative effect of the counter-rotating polarization on the dominant precession.

In fact, in this limit there is a natural correspondence with hopping models ubiquitous in condensed matter, as discussed in [16]. Just as precession of a gyroscope can exert torque on its neighbors to induce precessional motion, with an energy cost depending on the bond strength, so too electrons or other excitations can hop from one site to another site associated energy based on the coupling between sites. In this "tight-binding limit," in which ψ^L has a perturbative effect on the dominant ψ^R precession, we again see that all complex terms arise from the network geometry, meaning that *phase offsets* are introduced in the response of one gyroscope to another's displacement in a manner that depends on angles between adjacent bonds in the network [16]. In particular, the approximate equations of motion allow one to predict the evolution by considering only the magnitudes and phases of the dominant rotation at each site:

$$\omega\psi_i^R = \Omega_p\psi_i^R + \frac{\Omega_k}{2}\sum_{m\in N(i)}\left(\psi_i^R - \psi_j^R\right)$$

$$+ \frac{\Omega_k^2}{8\Omega_p}\left[-\sum_{j,j'}\left(\psi_i^R - \psi_j^R\right)e^{2i\theta_{j'ij}}\right.$$

$$\left. + \sum_{j,k}\left(\psi_j^R - \psi_k^R\right)e^{2i\theta_{ijk}}\right], \qquad (18)$$
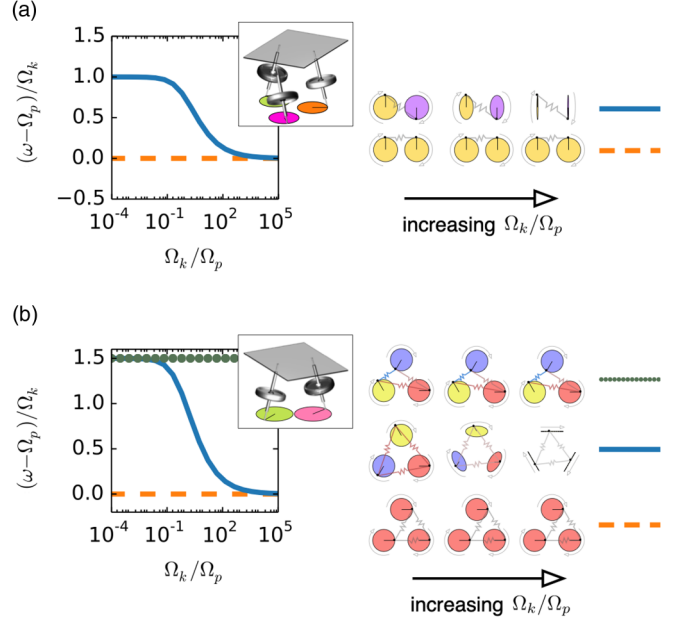

(a)

(b)

FIG. 5. Low interaction strength enables connection to tight-binding models by diminishing coupling between polarizations. In the limit that $\Omega_k/\Omega_p \to 0$, eigenmode frequencies of a gyroscope pair or triad approach the precession frequency, Ω_p. The slight deviations from Ω_p are proportional to Ω_k, resembling a tight-binding model with intersite coupling of $\Omega_k/2$ [Eq. (18)]. (a) Two modes represent a pair of gyroscopes' bonding and antibonding behavior. Decreasing the interaction strength decreases the ellipticity of the higher-frequency mode: the counter-rotating component presents only a small perturbation on the dominant clockwise motion. In the limit of $\Omega_k/\Omega_p \to 0$, both modes are nearly circular, like in quantum mechanical models with unitary evolution. Here the phase of the displacement is akin to the phase of a wave function. (b) For the gyroscopic triad, the oscillation frequency is Ω_p for the uniform precession ("ground state") mode and $\Omega_p + 3\Omega_k/2$ for the phased circular mode. The intermediate mode frequency varies as a function of Ω_k/Ω_p, interpolating between the two bounds. Only the intermediate eigenmode changes shape, becoming increasingly circular as the coupling strength weakens.

where the bond angle θ_{ijk} is the opening angle between bonds ij and jk, the first sum is over the N neighbors of i, and the subsequent sums are over pairs of neighbors j and j' of i and neighbors k of j for each of i's neighbors j. In this limit, the full equations of motion become more like a standard hopping model because they contain only one complex degree of freedom per site, ψ_i^R.

Note that the phase offsets of 2θ arise in the term proportional to $\Omega_k^2/8\Omega_p$. This complex next-nearest-neighbor coupling is reminiscent of phases from magnetic flux in common tight-binding models [2], but here the phases depend on the arrangement of the gyroscopes in space. Furthermore, the phase shifts arise here because of the counter-rotating polarizations, ψ^L, which are not present in the tight-binding picture. We stress that the complex-valued coupling encodes the fact that perturbing one gyroscope gives rise to a *phase-shifted* response at a nearby site, with a phase shift dictated by the geometric arrangement of the bonds. Thus, geometry provides phase shifts which generically break TRS except in

special circumstances such as a rectangular lattice, where all angles θ_{ijk} are multiples of $\pi/2$. As discussed below, it is these TRS-breaking terms that generate topological band gaps in gyroscopic networks.

III. REAL-SPACE INTUITION FOR BAND GAPS IN LATTICES

In this section we consider the spectral gaps that arise naturally in large collections of gyroscopes in ordered as well as amorphous configurations. We focus on the role of symmetry and local dynamics in determining their origin. We begin by examining the mechanical motions that underlie the frequency splitting of neighboring bands, linking these motions to TRS breaking through the coupling of left- and right-circular polarizations. We then study the evolution of the band structure as we tune the coupling between neighboring unit cells of gyroscope pairs, allowing us to contrast the topological gap origins with gaps created from bonding and antibonding behavior of isolated dimers. Last, we provide a simple method to predict the existence of band gaps without full diagonalization of a system's dynamical matrix.

A. Band gaps in the honeycomb lattice

A simple honeycomb lattice of gyroscopes has gaps in the system's bulk phonon spectrum, shown in the black band structure in Fig. 6(a). If the springlike coupling between sites is weak, the gap nearly closes at the corners of the Brillouin zone [orange spectrum in Fig. 6(a)]. As we increase the coupling, the gap broadens. Physically, gaps arise due to the coupling of left-polarized motion with the right-polarized motion of the gyroscopes, which breaks time-reversal symmetry in the dynamics [Eq. (14)]. Inspecting the honeycomb lattice's normal modes bounding the gap leads to an intuitive picture of this coupling's effect.

The lattice symmetry allows us to focus on a single hexagonal plaquette to fully describe the bulk excitations bounding the band gap. Figure 6(a) shows these modes bounding the gap, located at the corners of the Brillouin zone K and K'. In the higher frequency mode bounding the gap, one sublattice site precesses clockwise and the other does not move. In the lower frequency mode, on the other hand, the excitation is not completely localized to one of the two lattice sites: the other site precess counterclockwise with a small amplitude. The difference in this motion provides an intuitive way to explain the gap, as we detail in a multistep argument in Fig. 6 and Appendix B.

The crux of the argument is the relationship between energy and frequency given earlier in Eq. (11). The small counterclockwise displacement in the lower-frequency mode relaxes the cycle-averaged spring energy, and since the oscillation frequency ω is directly proportional to the average potential energy over a normal mode cycle, the frequency of this mode is smaller than the state with a truly immobile site (see Appendix B for details). This lower energy is evident from the force imbalance from the neighboring springs in the lower-frequency mode [Fig. 6(a)]. In contrast, for the higher-frequency mode, springs are stretched or compressed by the same amount around the B site, so there is no net force, and the center gyroscope does not move at all. This mechanical

mechanism for gap generation is different than in the Haldane model [2], where all excitation resides on only one of the two sublattice sites for both modes bounding the gap and the energy splitting arises purely from the next-nearest neighbor coupling.

In this case, the particular lattice symmetry of the honeycomb allowed us to make strong constraints on the shape of the mode displacements to explain the band gap (see Appendix B), but this is not always possible in general. In later sections, in discussing structures without translational order, we will provide alternative arguments for the existence of topological band gaps.

Increasing the spring coupling amplifies the frequency separation between the two states, broadening the gap and leading to larger and larger counterclockwise rotation on the B sites at K', as shown in Fig. 6(c). If, instead of increasing the spring coupling, we detune the precession frequencies at the two sublattice sites, the gap similarly broadens. However, the material in this case is a trivial insulator, and the motions of the two states bounding the gap remain unchanged as the inversion symmetry breaking grows, without any signature of coupling between right and left polarizations [Fig. 6(d)].

What have we learned? The coupling between right- and left-circular polarizations produces phase shifts between interacting gyroscopes, thereby breaking time-reversal symmetry, in a manner reminiscent of the simple three-gyroscope triad of Figs. 3–5. The spring forces directly induce counter-rotation because of the surrounding gyroscopes' phases. In turn, this coupling between the clockwise and counterclockwise states opens the gap by splitting the cycle-averaged spring energies, imparting an opposite chirality of precession between the two sublattice sites. In more general scenarios, we may not have such symmetric configurations near the gap, but the role of coupled polarizations and relative phases remains.

Importantly, if the dynamics were artificially modified to suppress the coupling between the left polarized (dominant for $\omega < 0$) and right polarized (dominant for $\omega > 0$) excitations, this splitting would not be possible, and no gap would emerge. That is, if we adjust the strength of block off-diagonal entries of the dynamical matrix that describe the coupling between clockwise and counterclockwise motion,

$$D = \left(\begin{array}{c|c} D_{LL} & \varepsilon D_{LR} \\ \hline \varepsilon D_{RL} & D_{RR} \end{array} \right), \tag{19}$$

so that $\varepsilon \to 0$, then the topological character of the bands vanishes. From Eq. (14) we recognize that this modification destroys any dependence of the dynamics on the geometry of the lattice, further highlighting the geometry-dependent topological phases that emerge. This right-left-coupling avenue for gap formation is distinct from inversion symmetry breaking, which instead adds only diagonal offsets to the dynamical matrix in D_{LL} and D_{RR}, with no mixing of polarizations.

B. From isolated fragments to a strongly coupled network

One way to disentangle local and global effects in an ordered system is to artificially partition it into subsections and study what happens as the partitions are coupled. We do this here with our gyroscopic lattice, showing that the
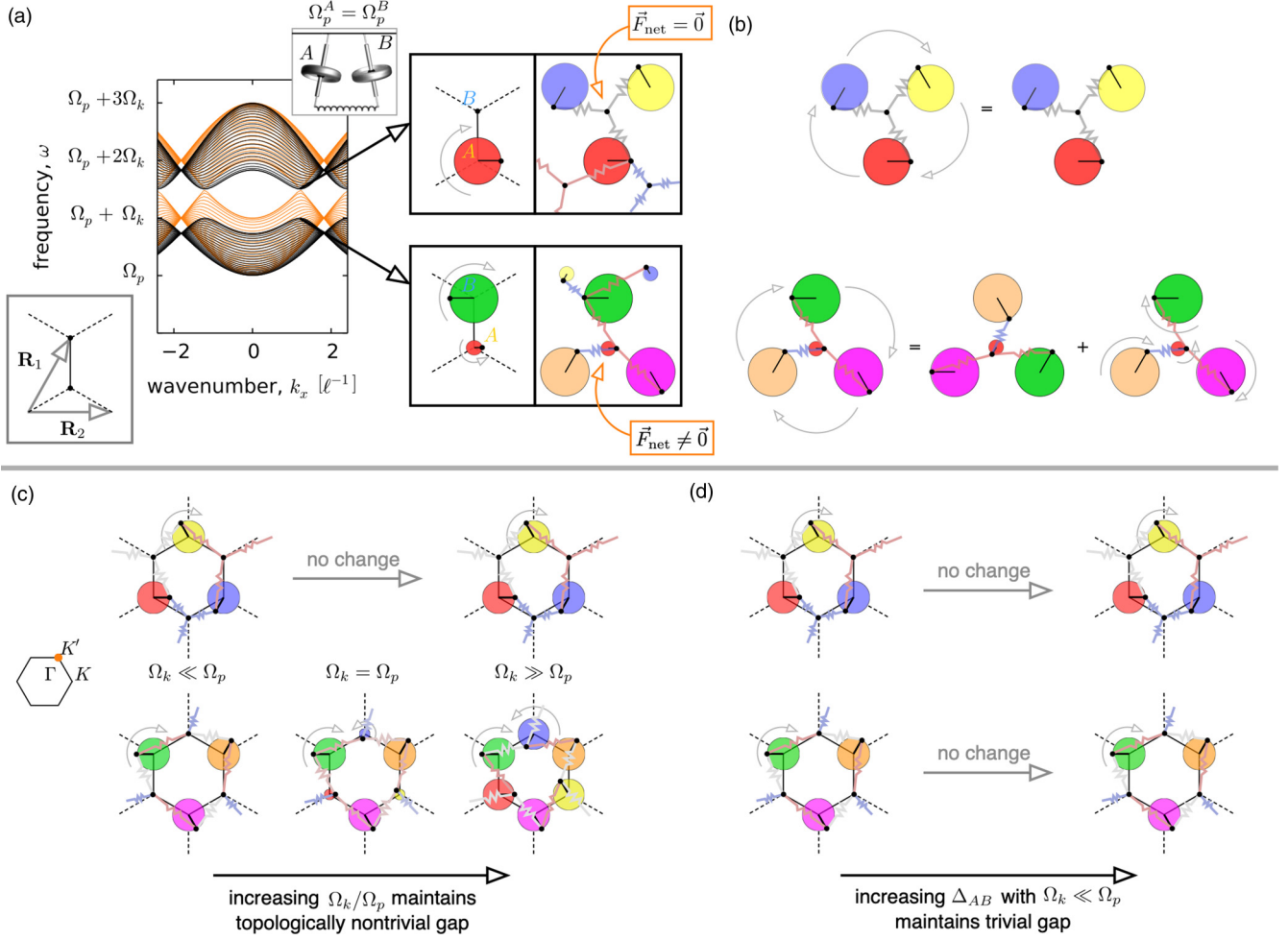
FIG. 6. Gyroscope mode displacements reveal how coupled circular polarizations lead to a gap. (a) The Dirac cones for the weak-coupling band structure (light orange bands) evolve into a band gap for the finite coupling case (black band structure), here shown for $\Omega_k = \Omega_p$. The point of closest approach lies at the wave vectors $\vec{k} = K$ or K', where the normal mode displacements take on a simple character: clockwise precession of one sublattice site and small (lower) or vanishing (upper) counterclockwise motion at the second sublattice site (left inset). Upon examination of the spring couplings connecting a unit cell to its neighbors (right insets), we find that spring forces cancel for the upper mode but do not cancel at the sublattice site with small excitation for the lower mode. (b) The geometry of these eigenmodes is determined by rotational symmetry at the K and K' points. Since a 120° rotation about any gyroscope must change the pattern only by a phase, all displacements must be purely circular. Furthermore, the state can either be invariant under rotation (upper panel) or else phase shifted with a counterclockwise rotation at the A site (lower panel). (c) For $\Omega_k \ll \Omega_p$, the two normal modes are asymptotically equivalent, up to an inversion of $A \leftrightarrow B$, since the smaller counterclockwise rotation on A vanishes in this limit. As the spring coupling increases, the counterclockwise excitation at the A site grows in magnitude, decreasing the spring energy and broadening the gap. In the limit of $\Omega_k \gg \Omega_p$ (rightmost images), the counterclockwise excitation magnitude approaches that of the clockwise excitation. (d) When the pinning frequencies at the two sublattice sites differ, so that $\Omega_p^A \to \Omega_p + \Delta_{AB}$ and $\Omega_p^B \to \Omega_p - \Delta_{AB}$, a trivial gap opens in the limit of $\Omega_k \ll \Omega_p$. Though the lower frequency state does not exhibit torque balance at the immobile sublattice site, the spring energy is negligible compared to Ω_p, so pinning torques dominate and no counterclockwise motion is observed. As a consequence, the excitation patterns bounding the gap do not change as the frequency splitting between the A and B sites grows.

topological gap cannot be understood as frequency splitting between bonding and antibonding behaviors, and we find analogous behavior in a familiar tight-binding model.

A pair of coupled oscillators will typically have a frequency splitting between bonding (in-phase) and antibonding (out-of-phase) behavior. Even in the presence of coupling between many such pairs of sites—which creates bands with a finite width out of the two localized modes of each pair—this fundamental origin of the two bands can be seen in the in-phase and out-of-phase character of eigenmodes. This results

in a local origin of band gaps in tight-binding systems, with a natural extension to the case of amorphous materials [34].

It is tempting to think that the two bands of our topological metamaterial seen in Fig. 6 may be continuously connected to in-phase bonding and out-of-phase antibonding behavior of gyroscopes in the unit cell. This, however, cannot be the case. We show this in Fig. 7 by considering a periodic honeycomb lattice with tunable coupling between unit cells, each of which consists of a pair of sites. We compare both the tight-binding and gyroscopic case, where the two-banded tight-binding
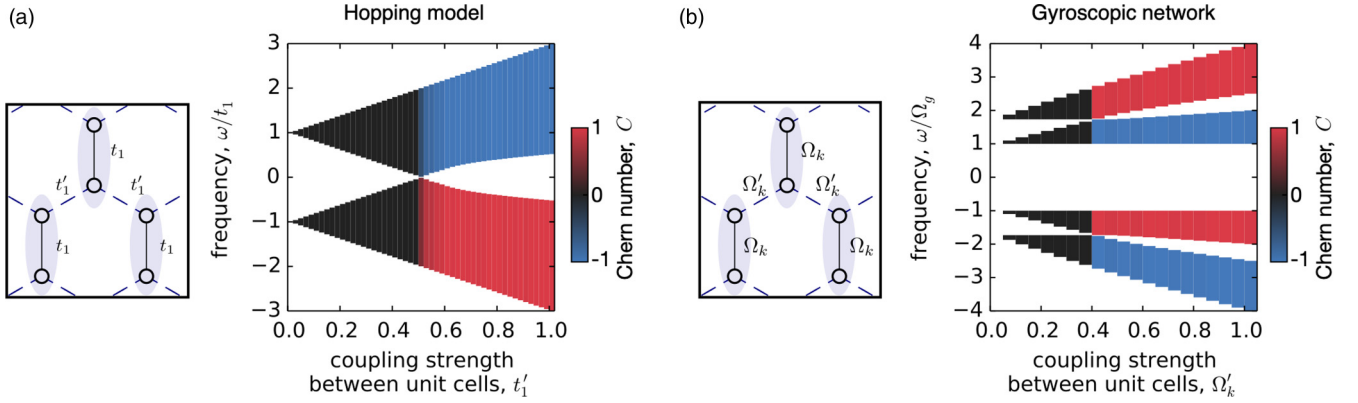
FIG. 7. The transition from isolated bonding and antibonding behavior to Chern insulating behavior in a Haldane-like tight-binding model mimics the analogous transition in gyroscopes. (a) Pairs of bonded sites or (b) gyroscopes are coupled to each other through bonds of varying strength (dashed lines). When the coupling is absent ($t_1' = 0$ or $\Omega_k' = 0$), the material is in a trivial insulating phase with one "bonding state," in which the excitations at site pairs are in phase, and one "antibonding state," in which the excitations are out of phase. These bonding and antibonding behaviors thicken into bands as the coupling is increased, until the two mix at the gap closing. Beyond this value, each band becomes topologically nontrivial, as marked by their nonzero Chern numbers $C = \pm 1$ (red and blue, respectively). The strength of complex next-nearest neighbor couplings, t_2, are controlled by the weakest link between next-nearest neighbors, which is t_1'. Here we set $t_2 = it_1'/10$. (b) The gyroscopic case, governed by the equations of motion given in Eq. (14), mimics the tight-binding picture, though there is a redundant copy of the positive frequency band pairs at negative frequencies.

dynamics analogous to Eq. (18) is given by the Haldane model of Ref. [2]:

$$H = -t_1 \sum_{\langle ij \rangle} c_i^\dagger c_j - t_2 \sum_{\langle\langle ij \rangle\rangle} e^{-i\phi_{ij}} c_i^\dagger c_j, \qquad (20)$$

where $\langle ij \rangle$ denotes nearest neighbors, $\langle\langle ij \rangle\rangle$ denotes next-nearest neighbors, $c_i^\dagger$ is the creation operator at site i, and $\phi_{ij} = -\phi_{ji}$ is a phase shift associated with hopping from site i to site j. By comparison with Eq. (18), we see that t_1 is akin to the coupling Ω_k between gyroscopes, t_2 is akin to $\Omega_k^2/8\Omega_p$, and ϕ_{ij} plays the role of the gyroscopic network bond angle $2\theta_{ijk}$. To tune between bonding and antibonding behavior within each pair of sites and topological behavior across the bulk, we vary the direct coupling t_1' between adjacent unit cells while keeping t_1 fixed for sites within a unit cell, and we set $t_2 = it_1'/10$.

If the bonds denoted by dashed lines are severed completely ($t_1' = 0$), the resulting network consists of isolated pairs of sites, each coupled by a bond of strength t_1 and uncoupled from other pairs. Such a system is a trivial insulator, akin to isolated molecular dimers in a lattice. As the dashed bonds are strengthened, the width of the two bands begin to broaden while remaining in the trivial insulator phase. The system transitions to a topological phase once $t_1' \approx 0.5$. Inspection of the eigenstates near the topological gap for $t_1' > 0.5$ reveals that the displacement patterns do not resemble simple bonding and antibonding patterns [refer back to the normal modes for $\Omega_k \ll \Omega_p$ in Fig. 6(c), which correspond to the case of $t_1' = t_1$]. How do we interpret this? For small t_1', the gap is formed by a frequency separation between bonding and antibonding behavior, while the gap with large t_1' arises due to the phase shifts enabled by coupling between clockwise and counterclockwise polarizations. Furthermore, the two phases have a macroscopic difference: the topological phase supports chiral edgemodes, indicated by the nonzero Chern number of each band. In Fig. 7 the colored bands exhibit nonzero

topological invariants of $C = +1$ (red) and -1 (blue), which we will define in depth in Sec. V. In short, by interpolating between the trivial and topological phases, we find that bonding and antibonding bands mix in order to open a topologically nontrivial gap.

The gyroscopic case is similar: trivial bonding and antibonding gaps are not continuously connected to the topological gaps from TRS breaking. As shown in Fig. 7(b), the spectrum of the gyroscopic honeycomb lattice with spring interactions resembles two copies of the Haldane model spectrum, one with $\omega > 0$ and another with $\omega < 0$, with symplectic symmetry relating the two copies. (Elsewhere in the paper, we omit the redundant, negative frequency states.) Varying Ω_k' between adjacent unit cells drives a topological phase transition, closing the gap generated by bonding and antibonding behavior of the coupled dimers. Once the gap reopens, the bonding and antibonding behaviors are mixed together, allowing topologically nontrivial bands and chiral edge modes in the gaps.

In this strongly interacting regime, the classic argument for the local origin of band gaps (like that of [34]) does not apply. This is because the physics of TRS breaking that opens the gap is distinct from the bonding and antibonding picture. The question is then: can we still predict whether there is a gap using a local argument, or do we have to compute the full band structure?

IV. BAND GAPS WITHOUT FULL DIAGONALIZATION

In the tight-binding limit discussed above in Sec. II E, the dynamical matrix simplifies. Within this framework, we consider three insightful forms of the dynamical matrix to understand the origin of band gaps.

The first form of dynamical matrix we consider is $D = D_{\text{diag}} + \delta$, where D_{diag} encodes the on-site energy in the electronic tight-binding picture (and the precession frequency of

the individual gyroscopes in the gyroscopic case). δ is a matrix of weak (as compared to the elements of D_{diag}) off-diagonal couplings. Schematically,

$$D \approx \begin{pmatrix} t_0 & & & & \delta \\ & -t_0 & & & \\ & & \ddots & & \\ & & & t_0 & \\ \delta & & & & -t_0 \end{pmatrix}. \qquad (21)$$

For $\delta \ll |t_0|$, the eigenvalues of D are simply close to the diagonal entries, and therefore gaps reside between different values of diagonal elements. In the example of Eq. (21), the eigenvalues bunch together around $\pm t_0$, and a spectral gap lies in between.

For trivial insulators with bonding and antibonding behavior, the dynamical matrix is not nearly diagonal, but can be arranged to be nearly block diagonal. The dynamical matrix of such a system appears in nearly block diagonal form, with all strong couplings contained within blocks and only small terms in the off-diagonal sectors:

$$D \approx \begin{pmatrix} 0 & t & & & \delta \\ t & 0 & & & \\ & & \ddots & & \\ & & & 0 & t \\ \delta & & & t & 0 \end{pmatrix}. \qquad (22)$$

As highlighted in the previous section, a system that can be divided into pieces, like our weakly coupled unit cells in a honeycomb lattice, generates two separated frequency bands from bonding and antibonding. The weak connections between the components broaden the spectrum by only a small amount, leaving the gap intact. This is similar to previous works in which a bond-centric description can explain why amorphous glasses have band gaps [34]. Note that in this case, though D is not nearly diagonal, D^2 *is* nearly diagonal.

Unlike either diagonal or block diagonal systems, a system with a topological band gap cannot be divided up into nearly independent pieces (Fig. 7; see also [35]). To transform a trivial gap into a topological one, couplings must be sufficiently strong to close and reopen the gap. From the perspective of the dynamical matrix, these strong off-diagonal couplings cannot be arranged in block diagonal form [35,36]. For example, the structure of such a dynamical matrix could follow the structure of Eq. (14), which we can roughly conceptualize as

$$D \approx \begin{pmatrix} 0 & \dots & t & \dots & it' \\ & & \ddots & & \\ -it' & \dots & t & \dots & 0 \end{pmatrix}, \qquad (23)$$

where large couplings t and TRS breaking terms it' are distributed throughout. One can certainly characterize band gaps by diagonalizing the Hamiltonian, but it would be useful to have a protocol for estimating whether a gap exists or what frequencies a gap may occupy without this costly step. For the case of a broad class of topological systems, we note that although D is highly nonlocal, D^2 is nearly diagonal, and we construct a method for estimating the gap in these systems below. This condition is closely connected to the condition of having a flat band, as occurs in crystal materials supporting the Fractional quantum Hall effect [37]. Such a protocol lends
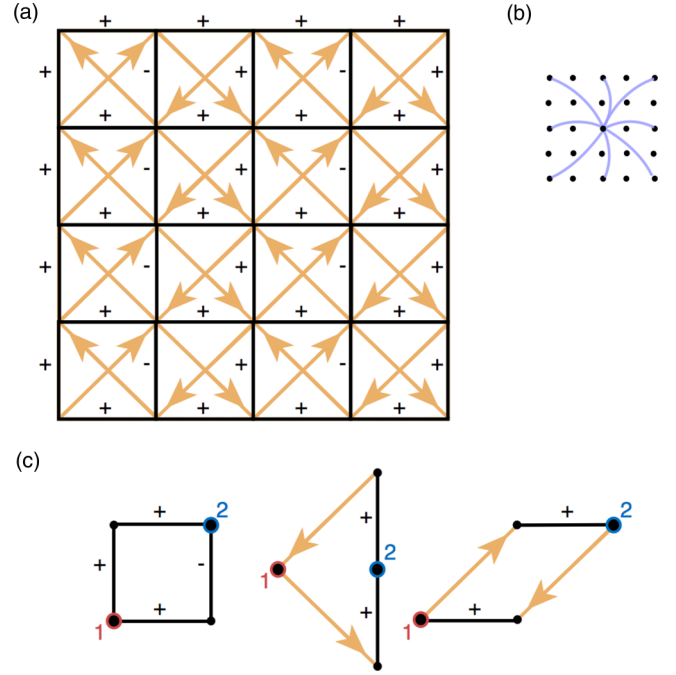

FIG. 8. The Chern number can be calculated by a local approximation in a square lattice model. (a) The model's dynamical matrix D is built from couplings $\pm t$ (solid lines) with the sign drawn on the picture. The gray diagonal lines have a coupling it' in the direction indicated by the arrows and $-it'$ in the opposite direction. (b) The square of the dynamical matrix, D^2, includes only horizontal and vertical couplings of two steps with matrix entry $t^2 - 2t'^2$ and diagonal couplings with matrix entry t'^2. Because of the phases in t, all the other matrix elements cancel out. (c) Examples of pairs of paths that cancel one another in calculating D^2 for the matrix element connecting site 1 (red) to site 2 (blue).

itself particularly well to understanding gaps in amorphous systems.

A. Existence of a band gap: Algebraic approach

Consider a system with a dynamical matrix D such that (1) some off-diagonal elements of D are large compared to on-diagonal elements—i.e., there are some couplings that are large compared to on-site pinning—and (2) the square of the dynamical matrix is nearly diagonal such that

$$D^2 = \omega_0^2 \mathbb{1} + \epsilon, \qquad (24)$$

where ω_0 is defined as the square root of the diagonal entry of D^2 and ϵ contains all the off-diagonal entries. We seek an argument that indicates whether a band gap exists without diagonalization of D.

Both conventional insulators with strong bonding and antibonding behavior and some topological systems meet these criteria, provided one subtracts a constant frequency so that the gap is approximately centered about zero. As an example with which to make the argument concrete, we will use one of the simplest systems with a Chern number, shown in Fig. 8.

This model comes from studying electrons in a square lattice in a magnetic field (a Hofstadter model) with a half unit of magnetic flux per unit cell. The diagonal couplings of strength

t' break time-reversal symmetry, opening the possibility of a topological band gap, while direct couplings are given a strength t.

We choose signs and phases of the couplings so that the sum of the phases of all the couplings going around each right triangle is $\pi/2$. Using this model, we find that the gap can be understood to result from interference during propagation of waves in the system, and a variational principle shows that this system has a gap for a range of values of the complex, next-nearest-neighbor coupling strength, t'/t. The method presented below can also in principle be applied to a system of gyroscopes.

We first show that there are both positive and negative eigenvalues (i.e., eigenvalues both above and below the net pinning frequency of an individual gyroscope). The value of $v^\dagger D v$ for any normalized vector v is an upper bound for the lowest eigenvalue of D if D is Hermitian, according to the variational principle. Similarly, for another vector u, $u^\dagger D u$ is a lower bound on the highest eigenvalue. One can choose in a variety of ways vectors v and u such that $v^\dagger D v$ is negative and $u^\dagger D u$ is positive, which forces there to be at least some positive and some negative eigenvalues. For example, let v be nonzero only on two adjacent sites of the network; the expectation value is either positive or negative for a suitable choice of relative phase between the two sites. This will be the case if there are off-diagonal elements that are larger than the diagonal elements of D—which is certainly true for the Hofstadter model, for which diagonal elements are zero.

Not only are there states with eigenvalues above and below zero, but furthermore these two collections of eigenvalues do not touch. To see this, recall that the *square* of the dynamical matrix has off-diagonal couplings that are small relative to diagonal ones: $D^2 = \omega_0^2 \mathbb{1} + \epsilon$. If the entries of ϵ are small compared to ω_0^2 the eigenvalues of D^2 must be close to ω_0^2, so D's eigenvalues must be close to $\pm\omega_0$, leaving a gap near 0. To make this argument more precise, we use a bound from Appendix C. From Eq. (24) it follows that the eigenvalues of D^2 are greater than or equal to $\omega_0^2 - \max_i \sum_j |\epsilon_{ij}|$. If this is positive, this ensures D has a gap whose width Δ is at least

$$\Delta \geqslant 2\sqrt{\omega_0^2 - \max_i \sum_j |\epsilon_{ij}|}. \tag{25}$$

Thus, the width of the gap is bounded by a quantity that does not require the diagonalization of D.

Intuitively, we can see that D^2 is nearly diagonal because of the effects of interference between paths in the Hofstadter model shown in Fig. 8. Each entry of D^2 is a sum $\sum_k D_{ik}D_{kj}$ over intermediate vertices k that have a nonzero coupling to both vertex i and vertex j. For the D given above, the entries of D^2 are shown in Fig. 8(b). Any pair of sites that are connected by a sequence of two bonds can in principle have a nonzero matrix element, but many of the couplings are zero because they cancel out [Fig. 8(c)].

The quantities in the estimate are $\omega_0 = 2\sqrt{t^2 + t'^2}$ and $\max_i \sum_j |\epsilon_{ij}| = 4|t^2 - 2t'^2| + 4t'^2$ so $\Delta \geqslant 4\sqrt{t^2 - |t^2 - 2t'^2|}$. If $|t'| < |t|/\sqrt{2}$, this bound is $4\sqrt{2}t'$, which is proportional to the size of the time-reversal symmetry breaking term, as expected. In this model, a gap in fact exists for any value of $t' \neq 0$, while this estimate

can be extended to prove the existence of this gap at least up to $|t'| = |t|$.

B. Green's function approach to estimating gaps

To better understand the connection of this argument to interference and locality, consider the Green's function $G(j, i; \omega) = [(\omega - D)^{-1}]_{ji}$, the amplitude of the oscillations of the jth site when the ith is oscillated by a unit force at a frequency ω. This shows how far energy is transported at a given frequency. We will show that this decays exponentially over a range of frequencies, implying that this range is a gap. [38].

First consider an ordinary insulator where there are two types of sites with different diagonal spring constants. Write $D = D_{\text{diag}} + \delta$, where D_{diag} includes the diagonal pinning frequencies and δ includes only the off-diagonal ones. The Green's function can be expanded in a geometric series as $\frac{1}{\omega - D_{\text{diag}}} \sum_{n=0}^{\infty} (\delta \frac{1}{\omega - D_{\text{diag}}})^n$. If ω is sufficiently far from the two diagonal entries, this series decays exponentially with distance. Let us imagine "bonds" drawn connecting any two sites with a nonzero value of δ. The first contribution to the sum for a pair of sites i and j appears at the mth term if it requires m steps to connect i to j along these bonds. The magnitude of this term decays as $(\max_{pq} |\delta_{pq}| / \min_p |\omega - D_{pp}|)^m$, with the rate of decay given by the ratio of the maximum off-diagonal component of D to the minimum on-diagonal component of $\omega - D$. This suggests that the Green's function decays exponentially. This argument leaves out a factor that counts the number of paths connecting a given pair of sites, but when this factor is included, we find that the Green's function does in fact decay exponentially when the off-diagonal terms are sufficiently small, as shown in Appendix D. Intuitively, with a short-range dynamical matrix, the network's energy transport is localized unless the couplings are large enough to be comparable with the difference between the applied frequency ω and the natural frequencies on the diagonal of D.

For our system, this argument at first appears invalid since the off-diagonal couplings are not small when gyroscopes are strongly coupled. A slight modification of this calculation does hold, however. For some forcing $\vec{f}$, the system responds in a manner determined by $\partial_t \psi_i = -i \sum_j D_{ij} \psi_j - i f_i$. Through repeated differentiation, we can find the derivatives of ψ_i in terms of the initial values of the ψ's, and typically higher derivatives depend on the displacement of more distant gyroscopes. This suggests that energy can be transported over long distances through chains of interacting sites. But if D^2 is almost diagonal, $\partial_t^2 \psi_i = -\sum_{jk} D_{ij}D_{jk}\psi_k - \sum_j D_{ij}f_j - i\partial_t f_i$, and the coefficient of ψ on the right-hand side is $D^2 = \omega_0^2 \mathbb{1} + \epsilon$, which is nearly diagonal. Physically, the disturbance produced by a given gyroscope mostly reflects back to itself after two steps due to interference. The solution to the equation for forces at a frequency ω (using vector notation) is

$$\psi = \frac{1}{\omega^2 - \omega_0^2 - \epsilon}(\omega + D)f$$

$$= \frac{\omega + D}{\omega^2 - \omega_0^2} \sum_{n=0}^{\infty} \left(\frac{\epsilon}{\omega^2 - \omega_0^2}\right)^n f, \tag{26}$$

which converges if ϵ's entries are small compared to $|\omega^2 - \omega_0^2|$, so the Green's function (the coefficient of f) decays exponentially with the distance.

Though no part of the topological system is disconnected from the remainder by weak couplings, interference can nonetheless suppress tunneling of excitation from a given region. This interference can arise over short paths or long length paths, depending on the details of the network. In the Hofstadter model we have used here, short paths of length two already generate significant interference, enabling a simple test to identify the band gap. In general, the interfering paths might be longer, requiring more and more terms in Eq. (26) to converge. Though the paths may be long, the series will necessarily converge for a suitable choice of parameters (see Appendix E). If there is a gap, this method identifies its existence if Eq. (26) converges, even in the case of topological systems with strong off-diagonal couplings.

We have discussed three cases. In trivial insulators with nearly diagonal D, we can predict the presence of a gap from the diagonal elements. Systems dominated by bonding and antibonding behavior are instead nearly *block* diagonal, and a gap will reside between bands of bonding and antibonding behavior. Third, topological systems require strong coupling between sites to drive the system into a different phase—one that cannot be described as a composite of noninteracting pieces. In this strongly coupled regime, interactions and eigenstates are nonlocal, threatening any prediction of band gaps without full diagonalization of the dynamical matrix [35,36]. Nonetheless, we constructed a simple argument if D^2 is nearly diagonal. As shown in Appendix E, this argument generalizes to a local method for finding locations of gaps even when D^2 is not nearly diagonal, since in such a case interference occurs between sufficiently long paths.

Our argument applies both to topological systems and other systems with strong couplings for which D^2 is nearly diagonal in the bulk. This point of view gives some insight into the origins of edge modes: near the boundary, D^2 is *not* nearly diagonal because some of the paths of force propagation that would interfere destructively are absent, and this delocalization allows for edge modes.

For disordered and amorphous samples, the denominators in Eq. (26) will sometimes be small, but the total expression may nonetheless decay in a similar manner to the Green's function of disordered trivial insulators [39].

V. MESOSCOPIC PROBES OF REAL-SPACE TOPOLOGY

Now that we have gained insight into how gaps arise, we turn to characterizing their topology. In particular, we seek local, real-space probes for global topological invariants. A natural starting point is the notion of flux pumping, which is a natural connection between a localized perturbation and a global consequence. After observing how flux-pumping plays out in a mechanical context, we review the traditional notion of the Chern number and its real-space generalizations in the form of the Kitaev sum and the Bott index. We compare these three methods of computing band topology and probe the extent to which we can approximate the Chern number using only the local structure of a network. Using a variant of the Kitaev sum, we find that, surprisingly, a purely local

computation can approximate the real-space generalization of the Chern number.

A. Flux pumping as a local probe for band topology

Arguably at the heart of band topology lies the notion of flux pumping [5]. In [23], we made a connection between flux pumping and real-space topology. Here we push this connection toward an even more local picture by considering small system sizes, finding that even amorphous patches ∼16 gyroscopes wide still possess clear signatures of flux pumping.

For an electronic Chern insulator, threading magnetic flux through the core of an annulus effectively transfers occupancy of edge states from one edge to another. On one boundary, the process pumps electronic edge states into the bulk conduction band and bulk states in the valence band onto the edge, while on another boundary, the process pumps edge states into the valence band and pumps bulk states in the conduction band onto the edge. With the goal of building a local description, we want to understand this topological phenomenon in terms of a localized perturbation. A localized phenomenon that is similar to pumping flux through an annulus arises when one quantum of magnetic flux is threaded through a small area in the bulk of the material. This localized insertion gives rise to a quantized charge accumulation at the site of flux insertion [23].

As magnetic flux is inserted into the bulk of the system, an induced electromotive force winds around the site. Given that a Chern insulator will exhibit Hall conductance, this induced field drives a current toward or away from the site of flux insertion, accumulating charge at the insertion site that is balanced at the outer boundary. Since the magnetic flux is related to the phase winding of electrons, magnetic flux can be simulated in the mechanical version of a Chern insulator by altering the interactions such that the force of one gyro j on its neighbor i is modified depending on the twisting angle θ_{twist}:

$$F_{ij} \sim \psi_i - \psi_j \rightarrow \psi_i - \psi_j e^{i\theta_{\text{twist}}}. \tag{27}$$

To give a concrete picture of how this could be built in an experiment, we envision attaching an extensible Hoberman ring to a small number of gyroscopes, as illustrated in Fig. 9(a). Each ring remains centered about the hanging axis of its gyroscope, so that when a gyroscope is displaced, the ring uniformly extends in all directions. The ring freely allows the gyroscope displacement to change in magnitude by expanding or contracting without any resistance and allows change in phase by rotating without any resistance. To twist the gyroscope i's response to its neighbor j, we affix the spring that couples i and j to a position on the ring offset from the gyroscope i's tip. This introduces a phase-shifted torque on the gyroscope. To mimic the effects of a gauge field, we are free to concentrate the modifications to the spring attachments along a radial cut of the annulus, shown as a blue dashed line in Fig. 9(a), effectively supplying a "twisted" boundary condition to the system along the cut of the annulus. If the spring joining gyroscope i to gyrosope j is affixed at a location on gyroscope j's ring ahead of its tip by an angle θ_{twist}, then the
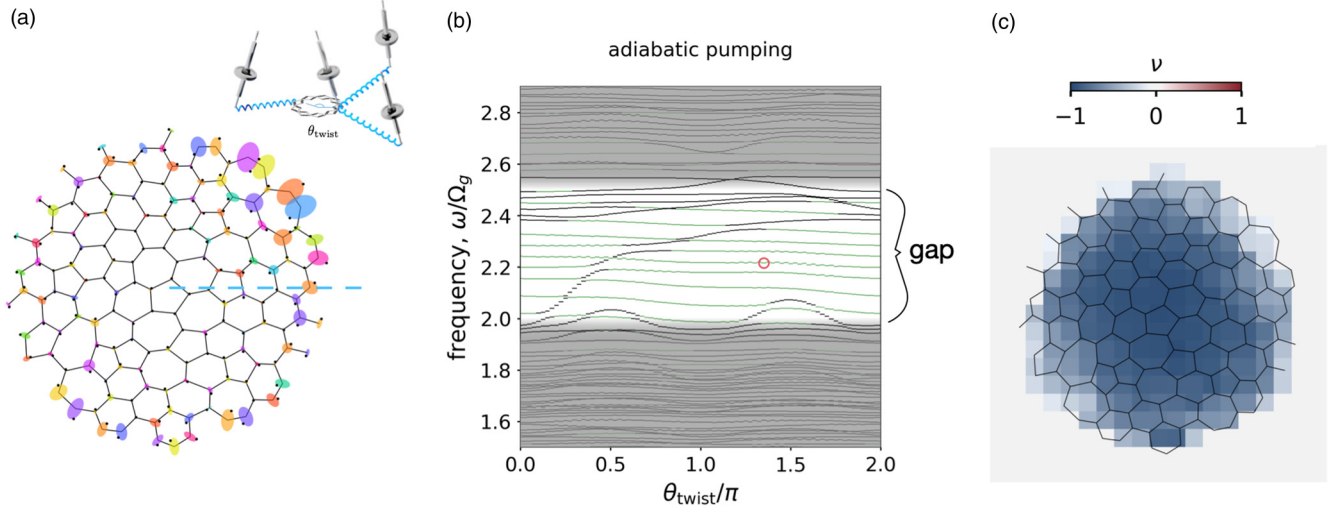
FIG. 9. The topological invariant in a small system can be measured by two related methods: the spectral response to twisted boundary conditions and the Kitaev sum. (a) Twisting the bonds along the dashed blue line by attaching an extensible ring to each gyroscope above the dashed line drives a phenomenon akin to flux pumping from a threaded magnetic field. The extensible ring, like a Hoberman ring, remains centered around the pivot point of the gyroscope and is free to rotate. This modulates the interaction by an angle, θ_{twist}. (b) Upon twisting the interaction angle by 2π rad, the spectrum returns to its initial state, but the nontrivial topology ensures that one state from the central region is pumped from the lower band to the upper band, while states localized to the outer boundary (green curves) are pumped towards the lower band. Here bands are shaded by a gray overlay. The red circle in the spectrum corresponds to the normal mode excitation shown in panel (a). (c) The Kitaev sum reveals that there is chiral conductance within the bulk of even a system $\sim$16 gyroscopes in extent. Here a region of summation half the size of the system is used to evaluate the sum at a grid of locations. The sum is proportional to the number of states at the system's core that are pumped from the conduction to the valence band.

force on gyroscope i from the interaction is likewise rotated $F_{ij} = -k/2[(\psi_i - \psi_j e^{i\theta_{\text{twist}}}) + e^{2i\theta_{ij}}(\bar{\psi}_i - \bar{\psi}_j e^{i\theta_{\text{twist}}})]$.

Twisting the bonds along the cut deforms the resulting band structure, but the system returns to its original state once the twist has taken the value $\theta_{\text{twist}} = 2\pi$. Figure 9(b) shows that during this operation, states localized to the outer boundary decrease in frequency [green curves in Fig. 9(b)], while a state localized to the center, where the effective magnetic flux resides, increases in frequency [black curve in the gap of Fig. 9(b)]. The net result of the operation is the exchange of one state between the two bands. Figure 9(b) highlights this action in the gap: the edge (green) states are transformed into adjacent, lower frequency states, while the state at the center of the sample (purple) pumps from the lower band to the upper band. In contrast, a trivial insulator has no exchange between the two bands, though extended states may be shuffled within each band separately.

Traditional treatment explains this phenomenon by looking at the band structure of the periodic bulk. We briefly review this more restrictive perspective before moving to a real-space point of view, where the lattice structure of the bulk is not needed and we are able to compute the band topology and understand flux pumping seen even for the small system shown in Fig. 9.

B. Real-space generalizations of Chern number

While flux pumping demonstrates a physical consequence of band topology even in small amorphous systems, there are compact mathematical quantities that capture the same information without tracking the flow of states. Historically, these were first defined in momentum space, but now several real-space generalizations exist that extend predictive power beyond crystalline materials. We will use these in two ways: (1) to define an approximate and purely local analytical expression for real-space topology in Sec. V C and (2) to characterize Anderson localization transitions in Sec. VI.

1. Traditional view: Berry curvature

The traditional point of view for computing band topology is to work entirely in reciprocal (momentum) space, which requires a crystalline material. While more restrictive, we briefly lay out this formulation in order to present the modifications in the projection operator that are required by symplectic symmetry. Here the Chern number for gyroscopes on a lattice is defined from the band structure of the equations of motion for small displacements. Diagonalizing the matrix describing the network's dynamics yields $2N$ frequencies of the dispersion bands at each value of $\vec{k}$, where N is the number of gyroscopes per unit cell. For each value of $\vec{k}$, each band has a corresponding eigenvector,

$$|\psi_j(\vec{k})\rangle = (\psi_1^R, \ldots, \psi_N^R, \psi_1^L, \ldots, \psi_N^L), \quad (28)$$

characterizing the amplitudes and phases of the N gyroscopes' collective motion. The symplectic symmetry of the dynamical matrix enables the eigenstates to be orthogonalized such that

$$\langle \psi_p | \cdot^\perp | \psi_q \rangle = \sum_\alpha \overline{\psi_{p,\alpha}^R} \psi_{q,\alpha}^R - \overline{\psi_{p,\alpha}^L} \psi_{q,\alpha}^L \quad (29)$$

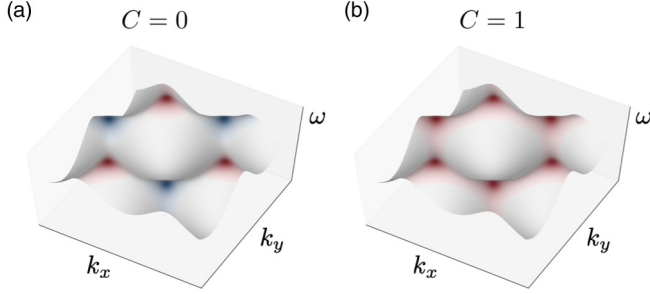$$= \delta_{pq} \, \text{sgn}(\omega_q), \quad (30)$$

FIG. 10. The Chern number is given by the integrated Berry curvature, which describes the connection between states in a band. (a) A topologically trivial band may have nonzero Berry curvature, but its integrated Berry curvature vanishes. (b) For a band with Chern number of $C = 1$, the integrated Berry curvature sums to 2π.

where α runs over each gyroscope and ω_q is the oscillation frequency of $|\psi_q\rangle$.

In a lattice, momentum space is periodic, just as the real-space lattice configuration is a tiling of the unit cell, implying that the Brillouin zone is a torus. Information about the connection of normal modes in each band is given by the Berry curvature, defined as

$$\vec{\Omega}_n = \mathbf{\nabla}_{\bar{k}} \times i\langle\psi|\mathbf{\nabla}_{\bar{k}}|\psi\rangle. \tag{31}$$

This Berry curvature is akin to a magnetic vector potential in momentum space, affecting the motion of wave packets as they traverse the system. The integral of the Berry curvature over the Brillouin zone describes the topological obstruction to a continuous connection between states in the band, encoded in the Chern number:

$$\int_{BZ} d\vec{S} \cdot \vec{\Omega}(\vec{k}) = 2\pi \, C. \tag{32}$$

The integer C is the Chern number of the band [6].

Figure 10 shows two schematic examples of a band colored by its Berry curvature. In Fig. 10(a), the Berry curvature is nonzero, but its integral over the Brillouin zone vanishes: this is a trivial insulator with inversion symmetry breaking. In Fig. 10(b), however, the contributions add, and the total value is a nonzero multiple of 2π. This nonzero Chern number signals the existence of the topologically protected chiral modes that live on the boundary of a system [6]. Topological protection ensures that, in the absence of available counter-propagating states, an edge wave will not scatter, passing around inclusions or voids and readily changing direction along jagged boundaries (Fig. 11).

An alternative representation of the Chern number uses the phase-invariant formula [40]

$$C_j = \frac{i}{2\pi} \int d^2k \, \text{Tr}[\partial_{k_\alpha} P_j P_j \partial_{k_\beta} P_j \varepsilon^{\alpha\beta}], \tag{33}$$

where C_j is the Chern number of the jth band, $\varepsilon^{\alpha\beta}$ is the antisymmetric Levi-Civita symbol, and P_j is the projection matrix defined for our system as

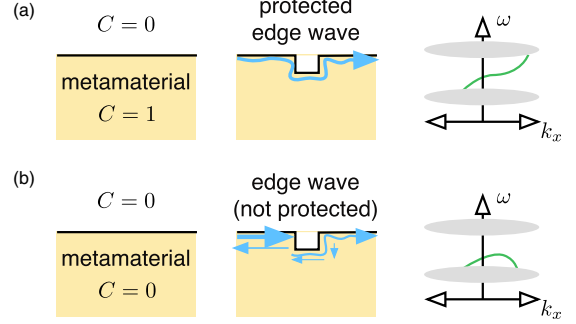$$P_j = |\psi_\alpha\rangle\langle\psi_\alpha|Q \, \text{sgn}(\omega_j), \tag{34}$$

FIG. 11. The Chern number counts the number of modes occupying a band gap. (a) In a system with a single gap and a single boundary, the number of right-moving modes—i.e., sets of possible eigenstates with positive group velocity—minus the number of left-moving modes is determined by the Chern number of a band. Nonzero Chern numbers give rise to topologically protected chiral edge modes, which are robust against back-scattering. (b) A topologically trivial insulator does not support protected edge modes on the boundary.

where

$$Q = \begin{pmatrix} \mathbb{I}_n & 0 \\ 0 & -\mathbb{I}_n \end{pmatrix}. \tag{35}$$

The factors of $Q \, \text{sgn}(\omega_j)$ arise from the symplectic structure of gyroscopes' equations of motion and the normalization of the states in Eq. (29). If the symplectic symmetry were ignored, and the projector was instead defined using a simple outer product of bands which were not orthonormal, a nonphysical distribution of Berry curvature would result, though this does not affect any of the computed Chern numbers. That is, the distribution of Berry curvature is altered, but the net curvatures are preserved. By using the symplectic formulation, the correct Berry curvature distributions are readily obtained.

Note that in previously reported results [16,23], this subtlety was overlooked. However, the results reported in these texts are unaffected because the net Berry curvature in each band with positive frequency is invariant without the symplectic form in the definition of the projector. Equation (18) of the supplementary information of [23], however, is incomplete, since the equation is missing factors of Q and $\text{sign}(\omega_j)$. The reported results of the Kitaev sum are nonetheless accurate because the set of all states $\langle\Psi|$ was taken to be the matrix inverse of the transpose of the set of states $|\Psi\rangle$, rather than just the set of conjugate transposes as the notation suggests, so that $P = |\Psi\rangle M \langle\Psi|$, where M is a matrix of ones along the diagonal for each state $|\psi\rangle$ of the set $|\Psi\rangle$ with frequency $\omega > \omega_c$ and zero for all other entries. Since the full matrix inverse was computed, the symplectic structure was implicitly taken into account—up to the sgn factor $\text{sgn}(\omega_j)$. Since all ω_c considered were positive, this sgn factor does not cause issues with previous results.

2. Kitaev sum

If disorder is present in a lattice or if a gyroscopic network has amorphous structure, translational symmetry is broken, and the Chern number previously described cannot be defined due to the absence of a Brillouin zone.
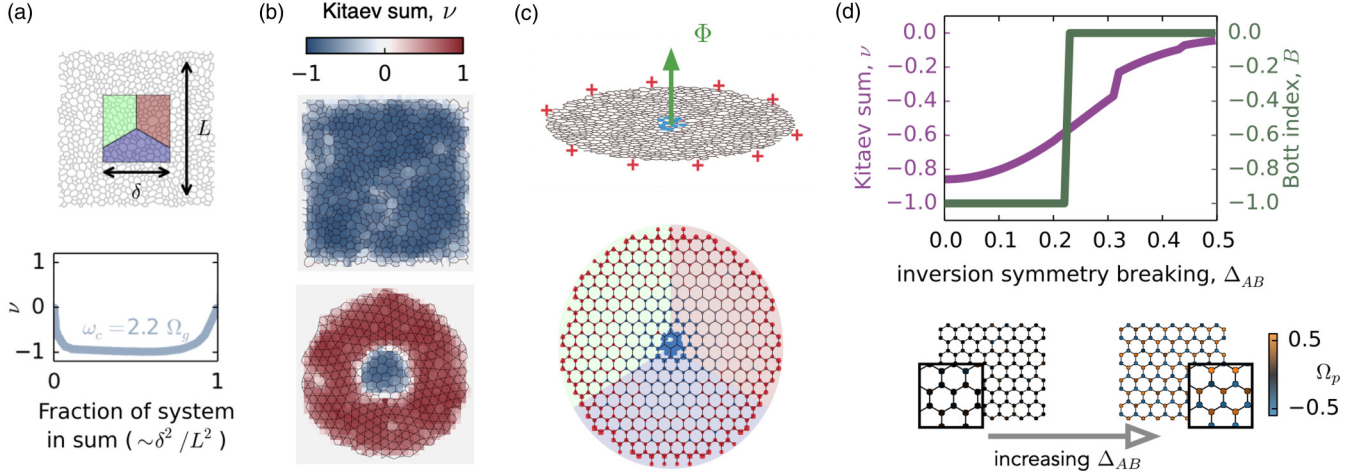
FIG. 12. The Kitaev sum and Bott index both measure band topology in real space. (a) The Kitaev sum measures the band-integrated spectral flow at a particular location in the bulk of the material. The sum converges to a target integer value corresponding to the Chern number of the system in the limit of an infinitely large system and large region of summation that does not enclose a boundary. The blue curve shows the convergence of ν for increasing sizes of the summation region δ. The projector used for this calculation maps all states of the amorphous system that are above $\omega_c = 2.2\Omega_g$ to themselves and maps states below ω_c to a zero vector. (b) Centering the summation region on different locations in an amorphous network in which all sites are trivalent (top) or in which two different local geometries are present (bottom) generates a spatially resolved measurement of the local topological character of the material. (c) In electronic systems, the Kitaev sum measures the net charge that accumulates near the location of magnetic flux insertion (top panel) [23]. In gyroscopic and electronic systems alike, the contribution to the sum is dominated by sites close to the site of flux insertion, represented by the large blue markers at the center of the circular sample. The size of each site's marker is proportional to the magnitude of the sum of terms in the Kitaev sum that include that site. Blue markers indicate a negative net contribution, while red terms indicate a positive contribution. An equal and opposite contribution resides on the boundary sites, mimicking the opposite charge that resides at the boundary in the electronic case, represented by the red markers at the edge of the circular sample. (d) The Bott index measures a topological obstruction preventing band-projected position operators from commuting. The index is a global measurement of band topology and requires closed boundary conditions. We contrast the Kitaev sum with the Bott index by studying a small gyroscopic honeycomb network subjected to inversion symmetry breaking. The Kitaev sum here has summation window set to include 45% of the sites in the system. The inset below in panel (d) shows the pinning strength at each site (ranging from blue to orange) for the samples used in the calculation with open (periodic) boundary conditions for the Kitaev sum (Bott index). The pinning strengths Ω_p of each site are disordered by adding an amount V sampled from a Gaussian distribution with a standard deviation of $0.1\langle\Omega_p\rangle$, and the gyroscopes have pinning strengths biased by their sublattice site: $\Omega_p = \langle\Omega_p\rangle(1 \pm \Delta_{AB}) + V$.

However, several real-space generalizations to the Chern number have been proposed. We discuss two approaches here. We use both to investigate topological phase transitions, and one will even enable us to build an approximation to the Chern number using only the local character of the network.

The Kitaev sum generalizes the notion of Chern number to a real-space measure of chirality integrated over a band in the bulk of a 2D material [23,41,42]. By defining a projection operator, P, that maps states above a cutoff frequency, ω_c, to themselves and states below the cutoff to zero, we obtain a real-valued number ν via

$$\nu(P) = 12\pi i \sum_{j\in A}\sum_{k\in B}\sum_{l\in C}(P_{jk}P_{kl}P_{lj} - P_{jl}P_{lk}P_{kj}). \quad (36)$$

The projection operator could instead be defined to map states *below* the cutoff ω_c to themselves, as is often done in electronic systems; in this case, $\nu \to -\nu$. When negative frequency bands are included, it is important to include the symplectic factors in Eq. (34). A, B, and C are three nonoverlapping summation regions defined in a counter-clockwise fashion as shown by the red, green, and blue regions of Figs. 12(a) and 12(c), and these can be of any shape.

In electronic systems, the Kitaev sum measures the charge that accumulates for a localized magnetic field flux inserted into the bulk position where the three regions A, B, and C meet. For a single magnetic flux quantum, the amount of charge is νe. In our gyroscopic system, ν similarly relates directly to flux pumping, signifying the number of states exchanged between the boundary and the site of flux insertion shown in Fig. 9(a) [23].

One feature of the Kitaev sum is that the result is not strictly integer-valued for a finite system. In the limit that the region of summation encloses many gyroscopes without enclosing the material's boundary, however, the value of ν does converge towards an integer, which corresponds to the Chern number. This integer counts the number of independent edge modes at the cutoff frequency ω_c spanning a spectral gap to connect surrounding bands. The proper counting of edge modes is a more subtle affair in the absence of crystalline symmetry, but can be done via the flux pumping analog considered in the previous section (see Fig. 9). This noninteger character of ν is useful in that the rate of convergence indicates the localization length of modes at the cutoff frequency: ν approximates its target value once the region of summation is larger than the localization length.

3. Bott index

An alternative approach which rests on K-theoretic methods is to measure what has become known as the Bott index [43]. Like the Chern number, a nonzero Bott index signals the impossibility of finding a complete, orthonormal basis of localized functions ("Wannier states") among the states included in the projection operator. Unlike the Kitaev index, the Bott index requires the construction of a periodic system, so translational invariance is artificially restored on some scale, though this scale can be made arbitrarily large. Given a fully periodic sample of spatial extent W in both spatial dimensions X and Y, the positions of each gyroscope are indexed by $\Theta = 2\pi X/W$ and $\Phi = 2\pi Y/W$. Equipped with a projection operator P as before, we define band-projected position matrices

$$Pe^{i\Theta}P \sim \begin{pmatrix} 0 & 0 \\ 0 & U \end{pmatrix}, \quad Pe^{i\Phi}P \sim \begin{pmatrix} 0 & 0 \\ 0 & V \end{pmatrix}, \qquad (37)$$

with the right-hand sides expressed in the basis of eigenmodes. If the cutoff frequency of P lies in a mobility gap, the block nonzero components U and V are almost unitary and will almost commute [43]. The Bott index, B, defined as

$$B = \frac{\text{Im}\{\text{Tr}[\log(VUV^{\dagger}U^{\dagger})]\}}{2\pi i}, \qquad (38)$$

indicates if U and V are "close" to a different pair of matrices which are exactly unitary and exactly commute. Since the logarithm is multivalued, Eq. (38) must be defined more precisely: we evaluate the sum of the logarithm of the eigenvalues of $VUV^{\dagger}U^{\dagger}$ and take the imaginary components to be as small as possible. A potential advantage of the Bott index over the Kitaev sum is that it returns an exact integer, rather than converging towards an integer value, at the cost of requiring the introduction of (potentially artificial) periodicity to the sample. A potential disadvantage is that the Bott index measurement is global: a given sample returns a single value, whereas the Kitaev sum can be performed in a spatially resolved manner [Figs. 9(b) and 12(a)–12(c)]. For a system composed of multiple patches of different topological phases, such as in the lower panel of Fig. 12(b), the Bott index selects only a single global readout.

C. Determining topology without full diagonalization

Given that such small systems can still be used to accurately compute real-space topological invariants and exhibit bulk-boundary correspondence, it is tempting to think that we can use the local properties of a network to approximate the topological invariant, under the assumption that the region is not exceptional. Here we will build on Kitaev's insight to address this challenge for systems that satisfy the same conditions as we required in Sec. IV: namely, that (1) some off-diagonal elements of D are large compared to on-diagonal elements and (2) the square of the dynamical matrix is nearly diagonal such that $D^2 \approx \omega_0^2 \mathbb{1} + \epsilon$. The goal is to approximate the projection operator, which is short-ranged [44,45]. This is a critical assumption behind the classification of interacting topological phases, which—like amorphous materials—are studied in real-space rather than momentum space.

To begin, we use an expression we derived in [23] that casts Kitaev's formula into

$$\nu = \text{Im}8\pi \sum_{ijk} P_{ij}P_{jk}P_{ki}, \qquad (39)$$

where P is the projection onto states below a given frequency, and the sum is over all sets of three points in the network that form a triangle surrounding a given point q in a counterclockwise orientation. This formula can be derived as the charge that accumulates when a magnetic flux quantum is threaded through q, and this expression translates directly into Kitaev's (and vice versa) if P is the exact projector. However, we will use an approximation to the projector, and Eq. (39) seems more reliable in the situation when P is known only approximately. Kitaev's formula requires a choice of subregions A, B, C that can change the value of the sum if P is merely approximated, but our expression requires no such choice.

The projection operator (or "projector") in a coordinate system where D is diagonal is $\sum_{\omega_n < \omega} |n\rangle\langle n|$ in the Hermitian case we are considering here, where ω_n are the frequency eigenvalues and $|n\rangle$ the eigenvectors. This is an inherently nonlocal object, but we can overcome this difficulty by writing the sum in an algebraic form as $\sum_{\omega_n} \frac{1}{2}(1 - \omega_n/\sqrt{\omega_n^2})|n\rangle\langle n|$, where the square root is the positive square root. Recast in a coordinate-independent way, $P = \frac{1}{2}(\mathbb{1} - D/\sqrt{D^2})$, which can be expanded using the assumption $D^2 = \omega_0^2 \mathbb{1} + \epsilon$, where ϵ is small, as

$$P = \frac{1}{2}\mathbb{1} - \frac{D}{2\omega_0} \sum_{n=0}^{\infty} \left(-\frac{\epsilon}{4\omega_0^2}\right)^n \binom{2n}{n}. \qquad (40)$$

Here we have used the Taylor series $\frac{1}{\sqrt{1-x}} = \sum_{n=0}^{\infty} \binom{2n}{n}(x/4)^n$. Substituting into Eq. (39), we note first that the first term ($\frac{1}{2}\mathbb{1}$) and its cross-terms with the other factors contribute only real terms to the sum because D is Hermitian and can therefore be neglected. Only the sum remains. If the $n = 0$ term dominates, then

$$\nu \approx \text{Im}\frac{\pi}{\omega_0^3} \sum_{ijk} D_{ij}D_{jk}D_{ki}. \qquad (41)$$

This is a local formula for the Chern number: since D_{ij} is short-ranged, the number of triangles ijk enclosing a point that contribute nonzero terms is limited.

A simple model both provides intuition and tests the accuracy of this result. For the Hofstadter model we considered before, which is associated with a gyroscopic network in the weakly interacting limit $\Omega_k/\Omega_p \ll 1$, ν is proportional to the product of the magnitudes of the couplings around the sides of a triangle times the sine of the net phase factor, normalized by ω_0^3. Intuitively, ω_0 is akin to a mean value of the coupling magnitudes, so this cancels out much of the dependence on the overall magnitude of the couplings, leaving mainly the dependence on the phases. For the square model, take q to be the point shown in Fig. 13(a). There are only two triangles surrounding q, which each contribute it^2t'. They are each counted three times, since the three vertices ijk can be enumerated with any cyclic permutation while retaining the
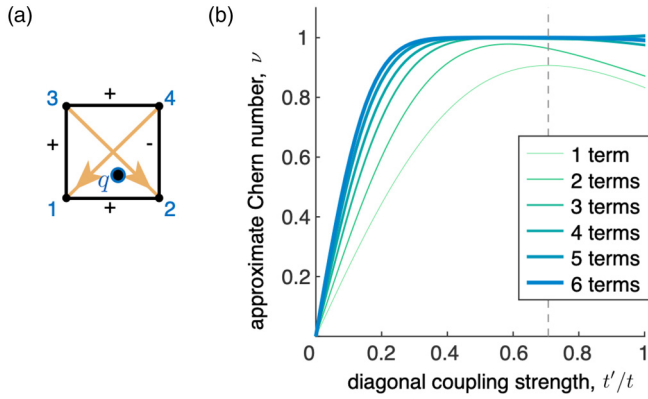
(a) (b)

FIG. 13. The Chern number can be approximated by a purely local, real-space calculation. (a) In the Hofstadter model, there are two three-hopping triangles formed from nonzero entries in D that encircle q, which are needed to calculate the lowest-order approximation to the Chern number. The two triangles are 123 and 124. (b) The approximation to the Chern number [Eqs. (39) and (40)] converges toward the true value of $\nu = 1$ as the number of terms included from the expansion of Eq. (40) grows. The thin green curve corresponds to the first term, given by Eq. (42), and thicker lines varying from green to blue indicate the result from including two, three, four, five, or six terms from Eq. (40). The measurement is shown here as a function of the complex, next-nearest-neighbor hopping strength t'/t (yellow arrows in panel a). The dashed, vertical gray line indicates the value of the ratio $t'/t = 1/\sqrt{2}$, where the approximation should be the most accurate. Above $t' > t$, the series does not converge for our choice of ω_0 in $D^2 = \omega_0^2 \mathbb{1} + \epsilon$. Note that the single-term approximation (thin green curve) reaches its maximum at this coupling strength, and further terms improve the result near $t'/t = 1/\sqrt{2}$.

proper counterclockwise ordering, so

$$\nu \approx \frac{3\pi t^2 t'}{4(t^2 + t'^2)^{\frac{3}{2}}}. \tag{42}$$

A true topological invariant should be quantized, but clearly this expression is not. We expect the approximation to work best when t' is close to $t/\sqrt{2}$ because for this value the next-nearest-neighbor entries in D^2 cancel. At this point, the approximation is $\pi/(2\sqrt{3}) \approx .9$, which is close to 1. A plot of the approximate Chern number against a range of complex hopping magnitudes t' in Fig. 13 is nearly constant for a range of values of t' near $t/\sqrt{2}$. Including more terms in the sum in Eq. (41) increases the accuracy of the Chern measurement in the vicinity of $t' = t/\sqrt{2}$. As discussed in Appendix E, convergence of the series requires ω_0 to be chosen so that ω_0^2 is at least as large as half the maximum eigenvalue of D^2. The method discussed here for computing a local approximation to ν generalizes to any system with a gap, regardless of whether D^2 is nearly diagonal, as we show in Appendix E.

This approximation to the real-space Chern invariant does not require a full diagonalization of the dynamical matrix. This result expands our computational machinery not only to predict if a gap will appear (as derived before), but also to predict if that gap will be endowed with chiral edge modes.

D. Mesoscopy versus homogeneity in determining topology

We have found that even in relatively small systems, a topological invariant can be readily approximated by the Kitaev sum without periodic boundary conditions. This demonstrates that band topology can be encoded on a mesoscopic scale—far smaller of a scale than has been traditionally investigated. If multiple topological patches are adjacent but uncoupled, then each patch will have its own edge states, but the system as a whole will not behave as a Chern insulator, since these states are distributed throughout the bulk. Since the "edge modes" of each patch occupy a frequency range that corresponds to the gap of a fully connected system, the material as a whole does not behave as an insulator. What degree of coupling between patches is required for these patches to behave as a single insulating system with chiral modes only at its outer boundary, rather than throughout its interior? Here we study the transition of weakly coupled mesoscopic patches of Chern insulator into a single unit of material.

Figure 14 shows patches of gyroscopic honeycomb networks bonded together by spring coupling with variable strength (dashed bonds in Fig. 14). With these bonds completely floppy ($\Omega_k' \ll \Omega_k$), the composite system is a trivial insulator, with a real-space Chern number measurement (here using the Kitaev sum) of $\nu \to 0$ (gray circles in the phase diagram of Fig. 14). If the coupling is strengthened, however, the material transitions to a Chern insulator at $\Omega_k' \approx 0.4\Omega_k$. Notably, so long as the patches are sufficiently large that the edge modes localized to their boundaries do not span the entire patch, the value of Ω_k' at the transition does not vary with patch size. Figure 14 shows the associated phase diagram: for cell sizes larger than $w \gtrsim 2\ell$, the transition from trivial ($\nu = 0$) to topological ($\nu = -1$) occurs at a constant coupling strength. This is an extension of our earlier observations in Fig. 7 in which varying the coupling between unit cells led to a topological phase transition at a critical coupling strength. There a sufficiently strong coupling ($\Omega_k' \approx 0.4\Omega_k$) was necessary to transform a trivial insulator of bonding and antibonding states into the delocalized states of a Chern insulator. Here, in addition, we find that even if large patches individually register as topological, a significant coupling is still required for the sample as a whole to have a nonzero topological invariant.

Below a critical coupling, the conductance of this gyroscopic material is not insulating on account of interior interfaces between insulating grains, reminiscent of the relationship between percolation and topological transitions (see [46] and references therein). This highlights the need for homogeneity in the coupling for a topological material to insulate throughout its bulk and highlights one of the ways in which topological insulation can break down in the presence of heterogeneity.

In the process of establishing a local origin of topological band gaps, we encountered the importance of homogeneity in the strengths of bonds throughout the bulk. Violating this assumption of homogeneity in couplings can change a material's topological phase. We now turn to the other way of breaking homogeneity in the bulk: modulating pinning strengths at each site. Consistent with our findings so far, we find that whereas inhomogeneity can break topological insulation, spatial order
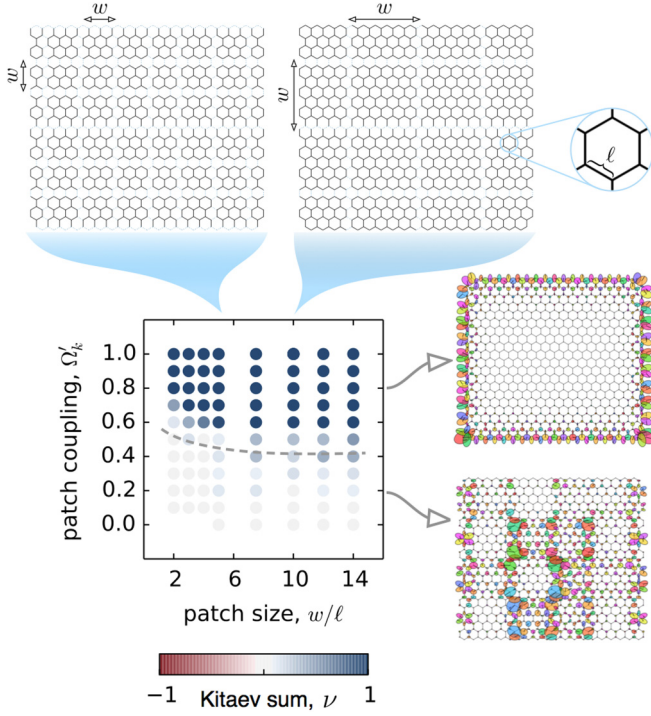
FIG. 14. In order for patches of Chern insulator to constitute a topological sample, the patches must be sufficiently coupled. By varying the spring constants connecting initially uncoupled regions of a gyroscopic network, we find that a threshold coupling strength is required to create a macroscopically topological sample. Here we used a 21×21-cell gyroscopic honeycomb configuration with $\Omega_g = \Omega_k$ and open boundary conditions. On the right side, two example eigenmodes with $\Omega'_k = 0.2\Omega_k$ and $0.8\Omega_k$ show the change in spatial structure of the excitations nearest $\omega = 2.25\Omega_p$ for patch sizes $w/\ell = 7.5$, where ℓ is the bond length. Below a critical patch coupling strength, edge modes span the boundaries between patches throughout the material, whereas above a critical patch coupling strength, a single edge mode resides on the outer rim of the network. The localization length ξ for a mode in the middle of the band gap is on the order of the bond length: $\xi \approx \ell$, with the precise value depending on the orientation of the boundary with respect to the lattice. So long as the patch size is greater than $\sim 2\xi$, the transition from trivial to topological occurs at a fixed coupling strength.

is utterly irrelevant to topological order. Indeed, in the final section of this article, we find that even in their response to on-site disorder, amorphous structures behave like their crystalline counterparts and undergo localization transitions consistent with the same scalings as in ordered crystals.

VI. SCALING AND REENTRANT TRANSITION OF ANDERSON LOCALIZATION

Topological insulators are famous for the chiral waves living at their edges for frequencies in the gap. However, there are also differences in the bulk modes at frequencies in bands bounding the gap. These modes can conduct energy in phononic metamaterials, where there is no Pauli exclusion and all modes are available excitations. For topologically trivial materials in two dimensions, any disorder is sufficient to localize all modes in a large enough system. For Chern

insulators, on the other hand, some normal modes in bands will be spatially extended across the entire system [36]. The study of how states localize in the presence of strong random disorder as a function of system size—the so-called scaling theory of "Anderson localization"–has provided a powerful framework to understand and predict the conductivity of a wide range of materials [39,47,48]. Recent extensions incorporate topological order into this scheme, giving rise to the notion of a "topological Anderson insulator" [49,50].

How do *amorphous* Chern insulators behave when subjected to strong disorder? In the first half of this section, we study the scaling of the topological index with system size, with particular attention to the amorphous case. By varying the disorder, we find behavior consistent with the expected scaling for symmetry class A, including annihilation of extended states in the mobility gap at the transition.

We then use inversion symmetry breaking to add a second dimension to this phase transition and find an avenue for disorder to drive a trivial insulating phase into a topological one. This reentrant topological behavior, dubbed "topological Anderson insulation," is surprising, since typically disorder drives systems away from the topological phase [51–53]. Using experiments and simulations, we identify this interesting feature of the interplay between disorder and topology in the mechanical context.

A. Anderson insulator transition

Strong disorder in pinning strengths drive a transition to the trivial insulating regime. In the canonical Anderson localization picture without any topological effects, the addition of infinitesimal disorder localizes all modes in a 2D system. In the presence of nontrivial topology, however, stronger disorder strengths are required to drive Chern insulators into the trivial insulating state. For small disorder, each band acquires tails of localized states, and bands carrying Hall conductance are confined to a region near the center of each band [leftmost panels in Fig. 15(a)]. As the disorder strength grows, these states approach and annihilate in a frequency region which was previously a mobility gap. This process is called "annihilation and levitation" due to the annihilation of the extended states in the gap and the subsequent rise in variance in the spacing between eigenfrequencies. In Fig. 15 we show that amorphous gyroscopic networks display this behavior as well.

Figure 15(a) shows this annihilation of extended states for amorphous networks of 450 gyroscopes. Without pinning disorder, the two bands of states which span the system are separated by a mobility gap. As we increase random pinning frequencies Ω_p drawn from a Gaussian distribution with width V, however, the extended states move toward the gap, meet in the frequency range which was previously the middle of the gap, and annihilate, shown in Fig. 15(a). Figure 15(b) shows that the localization length in the middle of the gap ($\omega \approx \Omega_p + 1.25\Omega_k$) rises as the extended states invade. The localization length peaks at a value near the system size, then falls as disorder dominates. The peak in localization length coincides precisely with the change in the ensemble-averaged topological index—whether Kitaev sum or Bott index—from nonzero to zero. Thus, the annihilation of the extended states mark the transition from a topological to trivial phase.
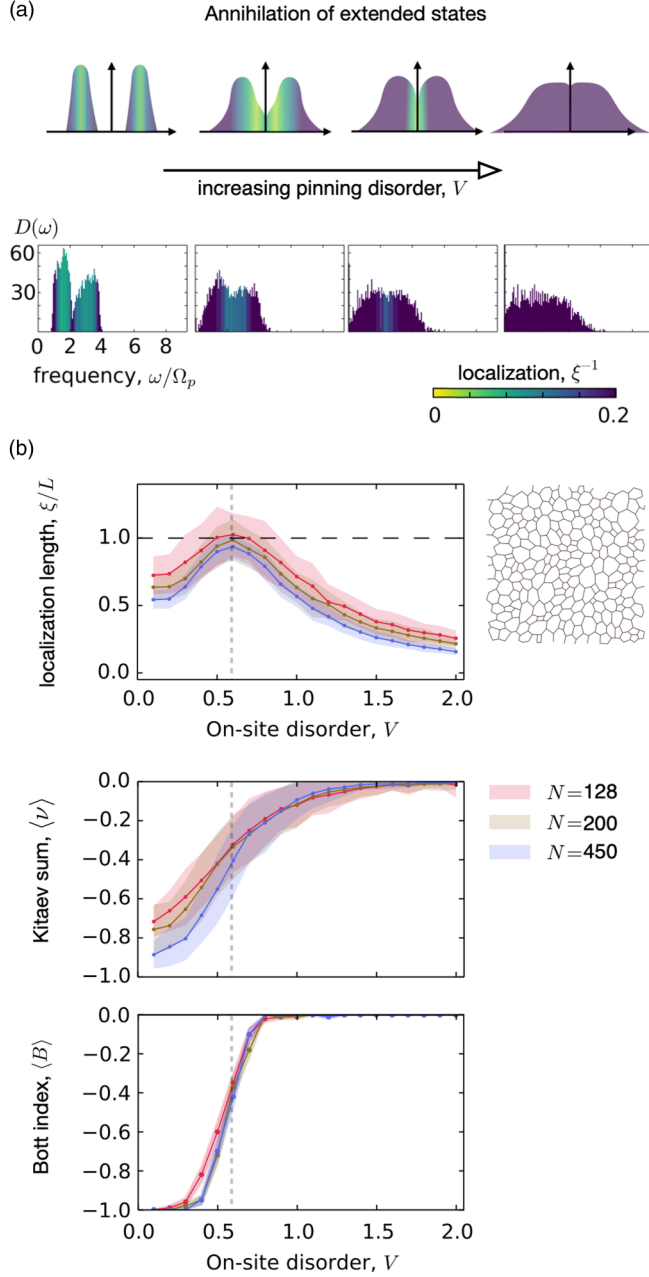
FIG. 15. Increasing disorder strength drives extended states towards the gap, where they annihilate as the system passes from a topological to a trivial insulator. (a) Illustration of the annihilation of extended states (yellow states) in the gap as pinning disorder strength V increases, as shown in a schematic cartoon (upper panel) and in computed spectra for a collection of 20 disordered amorphous gyroscopic networks of 450 gyroscopes (lower panel) with $\Omega_k = \langle \Omega_p \rangle$. The colors of these spectra reflect the localization of states, ξ, measured in units of inverse average bond length. These extended states (yellow) carry the Hall conductance for the system, so their annihilation triggers a transition to a trivial insulating phase, in which all modes are localized (purple). (b) We compute localization length and topological indices for a range of on-site disorder strengths for 20 amorphous networks such as the example structure shown on the right. As disorder grows, the localization length in the gap grows to the system size, aligning with the change in average topological invariant of the top band from -1 to 0. The vertical dashed line marks the disorder strength at which the topological transition occurs.

By measuring the topological invariant for systems of different sizes, we find sharper and sharper transitions to the trivial phase as the system size increases. Intuitively, a disordered topological system whose size is comparable to the localization length will be susceptible to random variations in disorder such that different realizations of disorder may yield a trivial phase. Near the transition, where the localization length of modes in the center of the gap is large, proportionally larger systems are required to suppress fluctuations in the resulting topological invariant. This is the case both for amorphous structures shown in Figs. 15 and 16, as well as for the honeycomb lattice we studied earlier. If the transition is perfectly sharp in the limit of an infinitely large system, then the system with disorder strength $V < V_c$ is a Chern insulator supporting topologically protected chiral edge modes, while systems with $V > V_c$ will register $\langle \nu \rangle \to 0$ and $\langle B \rangle \to 0$.

In Fig. 16 we compute the topological invariants for thousands of amorphous systems with different sizes and disorder strengths. After tracing out the average topological invariant as a function of disorder for many system sizes, we collapse these curves by rescaling the disorder strength according to

$$\tilde{V} = V_c + (V - V_c)\left(\frac{L}{L_0}\right)^{1/\tilde{\nu}}. \tag{43}$$

Here L is the system size, L_0 is an intermediate size, V_c is a critical disorder strength at which all curves should in principle intersect, and $\tilde{\nu}$ is the critical scaling exponent. Figure 16 shows that both the Kitaev sum (top panels) and Bott index (bottom panels) collapse under finite-size rescaling of Eq. (43) with the same values $V_c/\langle \Omega_p \rangle = 0.645 \pm 0.007$, and scaling exponent, $\tilde{\nu} = 2.80 \pm 0.18$, though small samples with fewer than 450 gyroscopes deviate visibly from this scaling due to boundary effects in the Kitaev sum. We note that while the Bott index data collapse has a sharp minimum in summed residuals (χ^2) that gives the reported uncertainties, the Kitaev sum collapse gives only loose bounds with uncertainties of order $\Delta\tilde{\nu} \approx 1$. The accepted value of $\tilde{\nu} = 2.58 \pm 0.03$ found in previous studies of quantum tight-binding models hugs our lower uncertainty bound [50,54].

The scaling collapse suggests that the transition is, in fact, infinitely sharp in the limit of large system sizes, with finite size scaling consistent with the universality class of Cartan label A [31]. This result is consistent with the idea that amorphous Chern insulators share similar scaling behavior with tight-binding models on lattices endowed with random pinning disorder [36,55]. Our system is also different from the traditional crystalline case in another way in that gyroscopic metamaterials are symplectic rather than Hermitian. It is interesting to note that neither difference appears to break the standard universal scaling [50]. While two recent studies have found nonuniversal behavior in amorphous systems [25,32], which motivates continued study of the scaling behavior along other directions of the phase boundary, we find no inconsistency with the scaling dictated by the symmetry class of the dynamical matrix.

B. Topological Anderson insulator phase diagram

We have seen that strong disorder destroys topological behavior. By tuning an additional parameter, however, we find
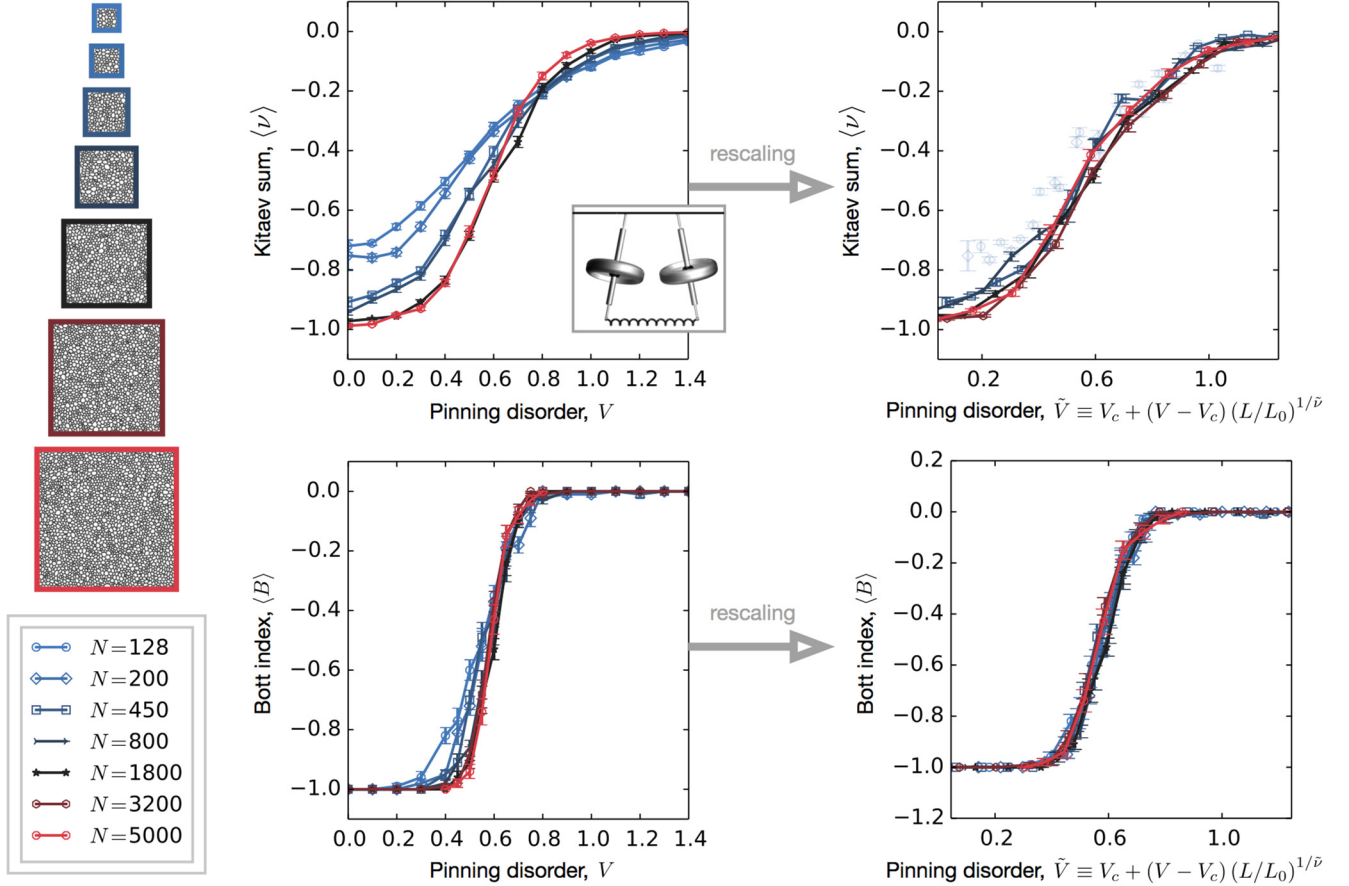
FIG. 16. Scaling collapse of the Anderson localization transition in our gyroscopic Chern insulators is consistent with the universality class of Cartan label A. As disorder is increased, the topological index of the upper band averaged over many samples smoothly varies from -1 to 0. The spatial structures of networks used here (left column) are Voronoi tessellations of hyperuniform point sets generated as in Ref. [23], with a gyroscope placed at every vertex and bonds lining the polygons of the tessellation. As the size of the system for which the index is computed grows (blue to black to red in each panel), the transition grows sharper. Each data point represents the average Kitaev sum $\langle \nu \rangle$ or Bott index $\langle B \rangle$ for 100 amorphous gyroscopic networks (10 disorder realizations for each of 10 randomly generated amorphous structures) subjected to on-site disorder strengths modulating Ω_p at each site by an amount taken from a Gaussian distribution. The pinning disorder strength is measured in units of $\langle \Omega_p \rangle$, and we let $\Omega_k = \langle \Omega_p \rangle$. Rescaling the disorder values according to a power law of the system size collapses the curves with an exponent $\tilde{\nu} = 2.80 \pm 0.18$ and $V_c = 0.645 \pm 0.007 \langle \Omega_p \rangle$, as shown in the right panels.

the remarkable possibility of transforming a trivial insulator into a Chern insulator simply by adding disorder to the system. Recently, this reentrant phase diagram of so-called "topological Anderson insulation" was demonstrated in photonic [52] and cold atom systems [53]. As shown in Fig. 17, gyroscopic metamaterials support this same transition. Here we simultaneously vary both random disorder strength and inversion symmetry breaking in a honeycomb lattice, both in experiment and in numerical calculations. We introduce disorder by changing the gyroscope spinning speeds, which changes both pinning frequencies and bond strengths simultaneously due to the dependence of each on spinning speed. Meanwhile, inversion symmetry is broken by a periodic array of staggered magnetic fields that splits the on-site precession frequencies of the two sublattice sites.

Figure 17(c) shows the resulting topological index, here shown by the Bott index averaged over 200 realizations for each value of disorder. Increasing either inversion symmetry breaking or disorder strength drives the gyroscopic lattice into the trivial phase, but increasing both simultaneously allows

for the topological phase to persist for significantly larger values of inversion symmetry breaking. This enables a reentrant phase transition by increasing disorder in a system with large inversion symmetry breaking. Using the Kitaev sum in place of the Bott index gives the same result, aside from weakened convergence near the phase boundaries. In Fig. 17(c) we choose $\Omega_k = 0.67\Omega_p$ to match the relative values in our experiment, and also choose the disorder to affect both pinning and interaction strengths proportionally, as would occur in an experiment. The qualitative features of the resulting reentrant phase transition, however, are indifferent to modest variations of these parameters, to the shape of the disorder distribution (flat versus Gaussian), and to whether or not interaction strength disorder is varied in tandem with pinning frequencies or instead of pinning frequencies.

Figure 17(d) shows complementary measurements made in an experimental setup of 54 gyroscopes coupled with repulsive magnetic interactions. Note that with magnetic interactions, the equations of motion are similar to the spring case considered thus far, as shown in Appendix A. The edge of the
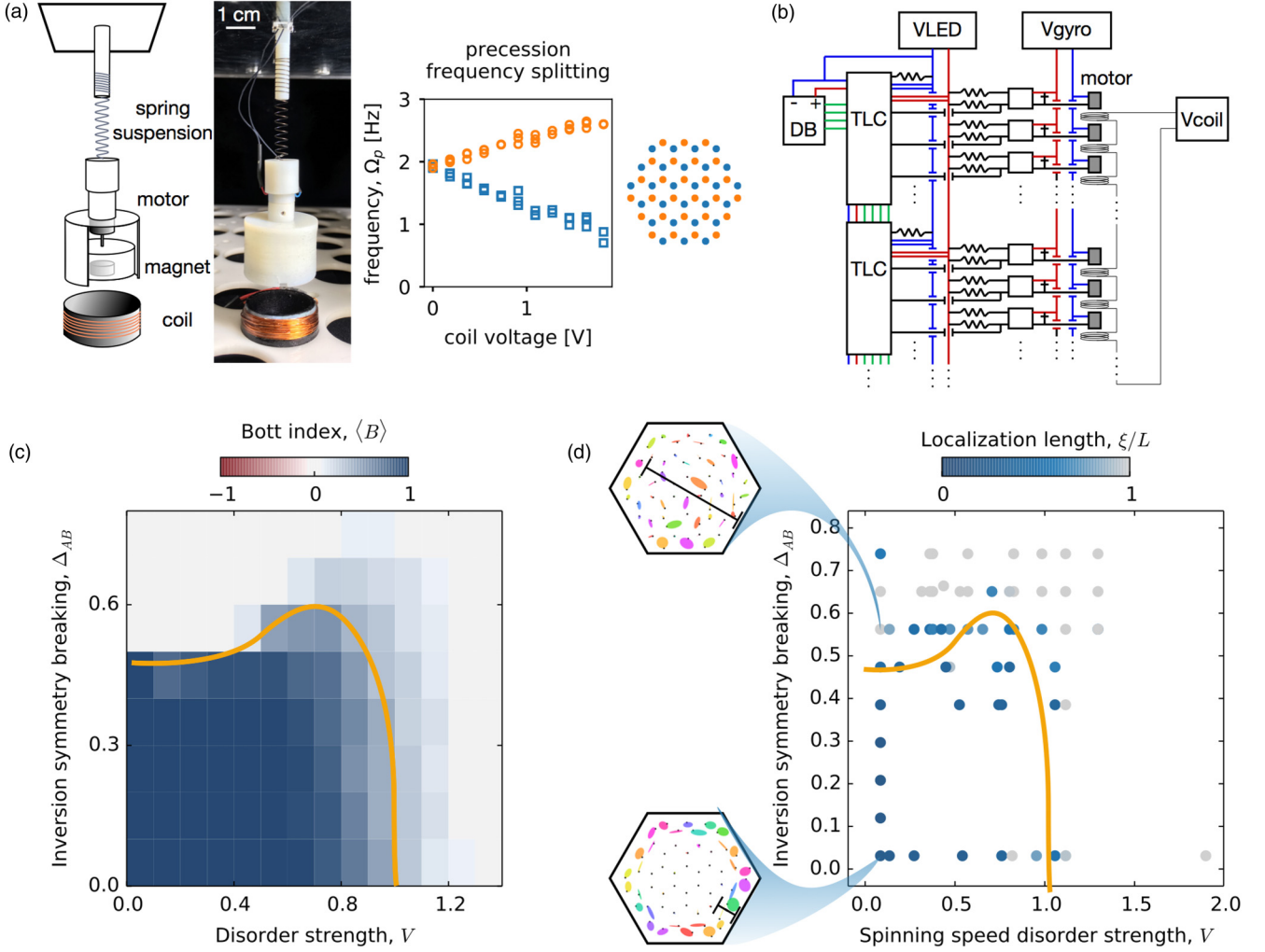
FIG. 17. Gyroscopic networks exhibit a topological Anderson insulator transition wherein a trivial insulator phase is driven into the topological phase by adding disorder. (a) In our experiments, each gyroscope is constructed from an externally powered motor encased in a 3D printed housing that minimizes damping. A magnetic coil placed beneath each site allows variation of the on-site precession frequency $\Omega_p \rightarrow \Omega_p \pm \Delta_{AB}$, with each sublattice site (orange and blue) receiving an opposite bias from the magnetic torque. (b) Daisy-chained microcontrollers (TLCs) convert a serial output into a site-specific spinning speed via pulse width modulation, while a separate DC power supply drives inversion symmetry breaking by passing current through each coil. (c) A 2D topological phase diagram shows that either breaking inversion symmetry (increasing Δ) or introducing strong disorder (increasing V) drives a transition from topologically nontrivial ($\langle B \rangle \neq 0$) to trivial ($\langle B \rangle = 0$). Each colored region represents the average Bott index computed numerically for 200 random disorder configurations with nearest-neighbor interactions only. The pinning frequencies are chosen from a flat distribution of disorder of width $V = [\max(\Omega_p) - \min(\Omega_p)]/\Omega_p^0$, and magnetic interaction disorder covaries with the pinning frequency, as would occur in the experiments. (d) An experiment designed to realize the topological Anderson insulator transition in 54 gyroscopes measures the localization length of normal modes excited in a frequency range within the band gap of the clean system ($\Delta = 0$, $V = 0$). As either disorder strength or inversion symmetry breaking is increased, the localization length grows on average, reaching or exceeding the system size, L. Disorder is introduced by controlling the spinning frequency of each gyroscope individually in a spatially uncorrelated fashion, which varies both pinning and interaction disorder strength. The orange line is a guide to the eye taken from simulations. Though the experimental system exhibits many differences from the numerical idealization, including long range interactions and strong nutation at low spinning speeds, the qualitative features of the transition are evident.

sample is shaken at a slowly varying frequency that spans the band gap range of the clean ($V = 0$) and inversion symmetric ($\Delta = 0$) system. Taking the Fourier transform of the tracked gyroscope displacements extracts the normal modes, from which we measure the localization length by fitting the displacement amplitudes to a decaying exponential as a function of distance from the edge. The average localization length ξ of modes in a narrow range of frequencies that lies in the gap of the clean system is reported as a fraction of the system

width, L. As the system approaches the boundary between topological and trivial phases, the localization length grows [gray dots in Fig. 17(d)]. In principle, the localization length should decrease again far from the phase boundary, though this subsequent decrease is not visible in our experiment except at low disorder.

In the experiments, the inversion symmetry is broken using a staggered array of magnetic coils, and the disorder strength is controlled by setting the spinning speeds of individual

gyroscopes using a chain of microcontrollers [Fig. 17(b)]. In our experimental setup, we set all experiments to have $\omega_0 = 175$ Hz spinning frequency, and we vary the width of the distribution using a pulse width modulation setup. Briefly, we first set all gyroscopes to have identical spinning frequencies by iteratively adjusting the duty cycle (i.e., fraction of time that a gyroscope is receiving power) assigned to individual gyroscopes using a pulse width modulation controller. This step cancels out initial disorder from variations in the construction of our 3D-printed and hand-assembled gyroscopes (Stratasys Objet 350 printer). We then generate a target spinning speed assignment for all gyroscopes so that the precession frequencies will approximately follow a flat distribution. We first attempt to achieve this assignment by perturbing the duty cycle values according to an average calibration relating duty cycle to spinning speed. We then iteratively measure the spinning speeds with a high-speed camera (Vision Research Phantom v12.1) and adjust the duty cycle values to approach the target spinning speed assignment.

There are several differences between the experimental realization and the idealized model. For large disorder strengths, some gyroscopes are set to spin very slowly. For these slowly spinning gyroscopes, nutation and nonlinear effects play a role in the dynamics, driving the system away from the fast-spinning-limit assumption. Additionally, the magnetic interactions are long range in the experiment. We choose to suppress both of these complications in the model shown in Fig. 17(c) to underscore the simplicity of the phenomenon.

We use the localization length as an indication of the phase transition rather than measuring the Chern numbers of the phases themselves. While this is an indirect measure of topology, the results capture the essential features of the expected phase diagram.

VII. CONCLUSION

Periodic order is dispensable for generating topology in gyroscopic metamaterials. In light of this observation, by reexamining the fundamental dynamics of coupled gyroscopes, we have identified intuitive, real-space descriptions for the origins of topological gaps. The signatures of time-reversal symmetry breaking—an essential ingredient in endowing bands with nontrivial topology—appear even at the threegyroscope level through the interaction of counter-rotating polarizations. The three-way interaction between TRS breaking, network geometry, and coupled polarizations underlies the emergence of topological gaps, and these nontrivial gaps are topologically disconnected from bonding and antibonding energy splitting. We present a method to predict the existence of a band gap without full diagonalization of the dynamical matrix that generalizes to amorphous structures. In the same spirit of simplifying the predictive machinery for topological phases irrespective of spatial order, we approximate the topological index using only local properties of a gyroscopic network, in contrast to other real-space methods in wide use. The ability to do so reflects the ability of even mesoscopic patches of gyroscopes to register as belonging to a topologically nontrivial phase, further supporting the notion that periodicity is not needed for nontrivial topology.

We find that disorder transitions in both amorphous and crystalline gyroscopic networks have similar behavior to periodic electronic and photonic Chern insulators. Amorphous networks display finite-size scaling that is consistent with the universal behavior from crystalline Chern insulators when subjected to pinning disorder on top of their existing structural disorder. Finally, we demonstrate a reentrant topological phase diagram in a mechanical context.

APPENDIX A: GYROSCOPES WITH MAGNETIC INTERACTIONS

If we replace the spring coupling with magnetic interactions as in Fig. 1(c), the equations of motion are modified slightly in the experimental system, which uses magnetic interactions rather than springs. In this case, the modified equation can similarly be cast in the form of Eq. (15) and appears as

$$i\partial_t \psi_i = \Omega_p \psi_i + \frac{1}{2} \sum_q \left[(\Omega_{ii}^+ \psi_i + \Omega_{ij}^+ \psi_j) \right.$$
$$\left. + e^{2i\theta_{ij}} (\Omega_{ii}^- \psi_p^* + \Omega_{ij}^- \psi_j^*) \right], \tag{A1}$$

where the sum is over nearby gyroscopes, $\Omega_{ij}^\pm \equiv -\frac{\ell^2}{I\omega}$ $(\partial F_{i\parallel}/\partial x_{j\parallel} \pm \partial F_{i\perp}/\partial x_{j\perp})$ is the characteristic interaction frequency between gyroscopes i and j, $\Omega_p \equiv (mg + F^{\text{suspension}} + F_z^{\text{coil}})\ell/I\omega$ is the precession frequency in the absence of other gyroscopes, and θ_{ij} is the angle of the bond connecting gyroscope i to gyroscope j, taken with respect to a fixed global axis. The interaction strengths, $\Omega_{ij}^\pm$, scale with the quantity $\Omega_k \equiv \ell^2 k_m/I\omega$, where k_m is the effective spring constant for the magnetic interaction, and $\Omega_{ij}^\pm$ depend nonlinearly on the lattice spacing.

APPENDIX B: NORMAL MODES AT THE BROKEN DIRAC POINT FOR THE GYROSCOPIC HONEYCOMB LATTICE

For the honeycomb lattice, we provide an argument for how symmetry determines the spatial structure of eigenmode displacements and their frequencies bounding the band gap. The two states at a corner of the Brillouin zone have frequencies

$$\omega = \left\{ \begin{array}{l} \pm \frac{1}{2}(2\Omega_p + 3\Omega k) \\ \pm \sqrt{\Omega_p(\Omega_p + 3\Omega_k)} \end{array} \right\}. \tag{B1}$$

Using the basis $\mathbf{e} = (\psi_0^R, \psi_1^R, \psi_0^L, \psi_1^L)$, the positive frequencies have eigenvectors

$$\mathbf{e}^+ = \left\{ \begin{array}{c} (1, 0, 0, 0) \\ \left(0, 1, \frac{-3\Omega_k}{2\Omega_p + 3\Omega_k + 2\sqrt{\Omega_p(\Omega_p + 3\Omega_k)}}, 0\right) \end{array} \right\}. \tag{B2}$$

For the pair of eigenvectors with larger absolute value of frequency, the excitations are solely ψ^R for $\omega > 0$ or solely ψ^L for $\omega < 0$. For the other normal mode pair with a smaller absolute value of frequency, the eigenvector is almost entirely in the opposite sublattice site, except for an excitation which is smaller in amplitude and opposite in chirality.

We can see how translational and rotational symmetry enforces the modes' form at K and K' in detail. First consider rotational symmetry of the lattice: $120°$ rotation preserve the momentum K or K' up to translation by a vector of the reciprocal lattice, so the modes at K and K' can be classified by their eigenvalue with respect to this operation. This eigenvalue is a phase factor, 1, $e^{i2\pi/3}$ or $e^{-i2\pi/3}$. Multiplication by a phase factor here corresponds to a displacement along the elliptical orbit of each gyroscope.

Equation (13) shows that multiplication by a phase, $\psi_p^R \rightarrow e^{i\theta}\psi_p^R$, $\psi_p^L \rightarrow e^{i\theta}\psi_p^L$, is equivalent to evolving in time by $\theta/\omega = \theta T/2\pi$, where T is the period of the mode. Hence rotational symmetry implies that the displacement pattern of the gyroscopes returns to itself if the whole system is rotated by $120°$ counterclockwise and then one waits by a time of 0, $T/3$, or $-T/3$. Consider specifically rotating $120°$ around one of the gyroscopes. Any ellipticity in the gyroscope's path would prevent the possibility that the rotated configuration returns to itself after some time. Thus, all nonzero gyroscope displacements must trace perfectly circular paths, either clockwise or anticlockwise.

Given that the orbits are circular, we can further constrain their pattern by considering the case of weak coupling compared to the pinning forces on each site ($\Omega_k \ll \Omega_p$). In this limit, the components of motion that are clockwise have a large amplitude compared to the counterclockwise components. At the K point, there are two modes, one in which the A sites have a strong clockwise motion and one in which the B sites have a strong clockwise motion. One could envision a mode in which all sites have a strong clockwise motion, but symmetry prohibits this as well, as we now show by considering one gyroscope moving with a small amplitude and the three gyroscopes around it moving with a large amplitude [Fig. 6(b)].

The relative phase of the three neighbors is determined by translational symmetry. Translating the excitation of an eigenmode by a lattice vector **R** merely introduces a phase

shift of $T\mathbf{k} \cdot \mathbf{R}/2\pi$. In Fig. 6, $\mathbf{R}_1$ and $\mathbf{R}_2$ are the two primitive vectors of the lattice. Any gyroscope located $\mathbf{R}_1$ away has a position that lags behind by a time $T/3$, and any gyroscope located $\mathbf{R}_2$ away leads by a time of $T/3$. Since these three gyroscopes are all moving clockwise, this means that in the first case the gyroscope will differ in phase by $2\pi/3$ counterclockwise from the reference gyroscope, and in the second it will be $2\pi/3$ clockwise. If the gyroscope with a small clockwise amplitude is at an A site [lower state in Figs. 6(a) and 6(b)], then this implies that the displacements of the neighboring B-gyroscopes rotate counterclockwise, while if it is at a B site, then the neighboring gyroscopes' displacements rotate clockwise as you go around the site clockwise [upper state in Figs. 6(a) and 6(b)]. As discussed in the text, this gives rise to a net force on the lower-frequency state and force balance on the immobile site of the higher-frequency state. A larger displacement at the counterclockwise site therefore lowers the spring energy for the lower state, opening the gap as Ω_k/Ω_p increases.

APPENDIX C: PROOF OF UPPER BOUND OF EIGENVALUES OF A MATRIX

Here we provide an upper bound on the eigenvalues of a hopping Hamiltonian used in the main text; it relates their magnitude to the sum of the hopping values from each site. To state this bound precisely, let M be a Hermitian matrix. Let $A = \max_i \sum_j |M_{ij}|$. Then if λ is any eigenvalue of M, $|\lambda| \leqslant A$. Let x be the eigenvector with eigenvalue λ. Let x's largest entry (in magnitude) be the kth entry. We have $\sum_j M_{kj}x_j = \lambda x_k$ by considering the kth entry of $Mx = \lambda x$. So

$$|\lambda||x_k| \leqslant \sum_j |M_{kj}||x_j|$$
$$\leqslant \sum_j |M_{kj}||x_k|$$
$$\leqslant A|x_k|. \tag{C1}$$

The first line follows by the triangle inequality, the second by the assumption that x_k is the largest entry in the vector and the third by the assumption that A is the largest of the sums of the absolute values of entries in a row of A. Cancelling $|x_k|$ gives $\lambda \leqslant A$.

APPENDIX D: EXPONENTIAL DECAY OF GREEN'S FUNCTION

In Sec. IV B, we argue that for a ordinary insulator, the Green's function expansion, which reads

$$\frac{1}{\omega - D_{\text{diag}}} \sum_{n=0}^{\infty} \left(\delta \frac{1}{\omega - D_{\text{diag}}} \right)^n, \tag{D1}$$

decays exponentially with distance. Here we provide more detail on this point. The largest contribution to the geometric series for the Green's function is from the shortest path connecting a given pair of sites. However, the main contribution to the Green's function could in principle be from longer paths, because although longer paths give a smaller contribution to the sum, there are many more paths that meander through

many sites from site i to j than direct paths. To give a rough (but rigorous) upper bound that takes this into account, note that there cannot be more than z^n paths of length n starting at site i if each site has z connections. In particular, there are not more than z^n paths connecting site i to site j in n steps. Therefore, the largest the Green's function can be is $\sum_{n=m}^{\infty}(z\alpha/\beta)^n$, where $\alpha = \max_{pq}|\delta_{pq}|$ is the maximum off-diagonal entry of the dynamical matrix, and $\beta = \min_p |\omega - D_{pp}|$ is the minimum on-diagonal component of $\omega - D$. This sum converges to a constant times $(z\alpha/\beta)^n$ if the off-diagonal elements are small enough. This shows that the Green's function decays exponentially. A similar argument can be used to show that the Green's function and projection operator are also localized for the topological insulator case based on the expansions in Eqs. (26) and (40).

APPENDIX E: LOCAL APPROXIMATION WITHOUT NEARLY DIAGONAL D^2

When a system has a dynamical matrix such that D^2 is nearly diagonal, it is possible to calculate its Green's function (within a gap) and the Chern number in a local way [see Eqs. (26) and (40)]. This expansion works also when D^2 is not close to a scalar, as long as the system has a gap (or probably even just a mobility gap). If one wants to find an eigenvalue close to a certain value, one can shift the diagonal entries of the matrix uniformly so that this value is at zero, square the matrix, and then use the Lanczos algorithm to find the minimal eigenvalue of the squared matrix [56,57]. In a similar way, we can find the Green's function near a given frequency. To calculate $(\omega\mathbb{1} - D)^{-1}$, square $\omega\mathbb{1} - D$ and then subtract a scalar, $\omega_0^2\mathbb{1}$, to make what remains as small as possible: $(\omega\mathbb{1} - D)^2 = \omega_0^2\mathbb{1} + \epsilon$. For a dynamical matrix whose square is nearly a scalar, ϵ is extremely small. However, it is possible that a dynamical matrix does not nearly square to a scalar, and here we generalize our earlier result to this case.

Physically, if $\epsilon = (\frac{(\omega\mathbb{1}-D)^2-\omega_0^2\mathbb{1}}{\omega_0^2})$ has large entries, then interference effects fail to keep an excitation localized within only two steps. Yet interference may arise between sufficiently long paths; correspondingly, the entries of higher powers of ϵ start to decay exponentially. One can then expand the Green's function, $(\omega - D)^{-1} = (\omega\mathbb{1} - D)(\omega_0^2\mathbb{1} + \epsilon)^{-1}$ by using a geometric series to calculate the reciprocal. This *always* occurs for the right choice of ω_0, as long as ω is in a gap.

The Chern number of the states above a frequency ω can be calculated in the same way. The Kitaev sum depends on

the projection, which we express as $P = \frac{1}{2}\mathbb{1} + \frac{1}{2}\frac{\omega\mathbb{1}-D}{\sqrt{(\omega\mathbb{1}-D)^2}}$. The square root can be expanded just as the Green's function was (the radii of convergence of the binomial expansion of $\sqrt{\omega_0^2 + x}$ and of $(\omega_0^2 + x)^{-1}$ are identical), giving

$$P = \frac{1}{2}\mathbb{1} + \frac{\omega - D}{2\omega_0}\sum_{n=0}^{\infty}\left(-\frac{\epsilon}{4\omega_0^2}\right)^n\binom{2n}{n}. \qquad (E1)$$

Let us argue that there is always a value of ω_0 such that this converges. The eigenfrequencies of D are contained in two intervals, $[M_1, \omega - \Delta_1]$, and $[\omega + \Delta_2, M_2]$, where Δ_1, Δ_2 are the distances to the edges of the bands, and M_1, M_2 are the minimal and maximal frequencies. Thus the eigenvalues of $(\omega - D)^2$ are all contained between $\kappa = \min(\Delta_1^2, \Delta_2^2)$ and $K = \max((M_2 - \omega)^2, (\omega - M_1)^2)$. Let ω_0^2 be the center of the spectrum, $\frac{1}{2}(\kappa + K)$, and define ϵ as above. Then ϵ's eigenvalues are between $\pm\frac{1}{2}(K - \kappa)$, which is less than $\omega_0^2 = \frac{1}{2}(K + \kappa)$ because $\kappa > 0$, and thus the expansion converges.

This argument has thus far relied on computing the range of eigenvalues. However, our goal is to calculate the projection and the Chern number without diagonalizing the dynamical matrix. To connect to our aim, we can note that if the terms of the series decay exponentially in the basis of eigenvectors, then they also decay exponentially in real space. One can find a useful value for ω_0 by calculating the terms of the series in real space for different ω_0's until one finds that it converges.

The argument above shows that the series must converge so long as there is a gap. In fact, large values of ω_0 always lead to a convergent series if a gap exists: in particular, values of ω_0 such that $\omega_0^2 > \frac{1}{2}K$ guarantee convergence if a gap exists. As a consequence, checking for convergence with $\omega_0^2 > \frac{1}{2}K$, where K is any upper bound on the spectrum, immediately signals whether there is a gap (in which case the series converges) or there is no gap (in which case the series does not converge).

The limitation of this approach is that the convergence can be slow, requiring a numerical approach. Slow convergence could result if the bands are wide compared to the gap or if there are many other bands besides the two bands bounding the gap. This is the case, for example, for gyroscopic lattices, in which there is a particle-hole symmetry that results in an asymmetric distribution of bands around any positive-frequency gap. In such situations, the convergence improves if one applies a polynomial to D to fold the spectrum so that the bands on each side of ω bunch together in frequency.

[1] J. M. Kosterlitz and D. J. Thouless, Ordering, metastability and phase transitions in two-dimensional systems, J. Phys. C **6**, 1181 (1973).

[2] F. D. M. Haldane, Model for a Quantum Hall Effect Without Landau Levels: Condensed-Matter Realization of the Parity Anomaly, Phys. Rev. Lett. **61**, 2015 (1988).

[3] T. Sanchez, D. T. N. Chen, S. J. DeCamp, M. Heymann, and Z. Dogic, Spontaneous motion in hierarchically assembled active matter, Nature **491**, 431 (2012).

[4] C. Coulais, D. Sounas, and A. Alù, Static non-reciprocity in mechanical metamaterials, Nature **542**, 461 (2017).

[5] R. B. Laughlin, Quantized Hall conductivity in two dimensions, Phys. Rev. B **23**, 5632 (1981).

[6] D. J. Thouless, M. Kohmoto, M. P. Nightingale, and M. den Nijs, Quantized Hall Conductance in a Two-Dimensional Periodic Potential, Phys. Rev. Lett. **49**, 405 (1982).

[7] E. Prodan and C. Prodan, Topological Phonon Modes and Their Role in Dynamic Instability of Microtubules, Phys. Rev. Lett. **103**, 248101 (2009).

[8] M. Z. Hasan and C. L. Kane, Colloquium: Topological insulators, Rev. Mod. Phys. **82**, 3045 (2010).

[9] S. Ryu, A. P. Schnyder, A. Furusaki, and A. W. W. Ludwig, Topological insulators and superconductors: Tenfold way and dimensional hierarchy, New J. Phys. **12**, 065010 (2010).

[10] C. L. Kane and T. C. Lubensky, Topological boundary modes in isostatic lattices, Nat. Phys. **10**, 39 (2013).

[11] R. Süsstrunk and S. D. Huber, Observation of phononic helical edge states in a mechanical topological insulator, Science **349**, 47 (2015).

[12] M. C. Rechtsman, J. M. Zeuner, Y. Plotnik, Y. Lumer, D. Podolsky, F. Dreisow, S. Nolte, M. Segev, and A. Szameit, Photonic Floquet topological insulators, Nature **496**, 196 (2013).

[13] J. Paulose, A. S. Meeussen, and V. Vitelli, Selective buckling via states of self-stress in topological metamaterials, Proc. Natl. Acad. Sci. USA **112**, 7639 (2015).

[14] A. S. Meeussen, J. Paulose, and V. Vitelli, Geared Topological Metamaterials with Tunable Mechanical Stability, Phys. Rev. X **6**, 041029 (2016).

[15] A. Souslov, B. C. van Zuiden, D. Bartolo, and V. Vitelli, Topological sound in active-liquid metamaterials, Nat. Phys. **13**, 1091 (2017).

[16] L. M. Nash, D. Kleckner, A. Read, V. Vitelli, A. M. Turner, and W. T. M. Irvine, Topological mechanics of gyroscopic metamaterials, Proc. Natl. Acad. Sci. USA **112**, 14495 (2015).

[17] N. P. Mitchell, L. M. Nash, and W. T. M. Irvine, Realization of a topological phase transition in a gyroscopic lattice, Phys. Rev. B **97**, 100302(R) (2018).

[18] N. P. Mitchell, L. M. Nash, and W. T. M. Irvine, Tunable band topology in gyroscopic lattices, Phys. Rev. B **98**, 174301 (2018).

[19] P. Wang, L. Lu, and K. Bertoldi, Topological Phononic Crystals with One-Way Elastic Edge Waves, Phys. Rev. Lett. **115**, 104302 (2015).

[20] M. Brun, I. S. Jones, and A. B. Movchan, Vortex-type elastic structured media and dynamic shielding, Proc. R. Soc. A **468**, 3027 (2012).

[21] G. Carta, M. Brun, A. B. Movchan, N. V. Movchan, and I. S. Jones, Dispersion properties of vortex-type monatomic lattices, Int. J. Solids Struct. **51**, 2213 (2014).

[22] R. Süsstrunk and S. D. Huber, Classification of topological phonons in linear mechanical metamaterials, Proc. Natl. Acad. Sci. USA **113**, E4767 (2016).

[23] N. P. Mitchell, L. M. Nash, D. Hexner, A. M. Turner, and W. T. M. Irvine, Amorphous topological insulators constructed from random point sets, Nat. Phys. **14**, 380 (2018).

[24] A. Agarwala and V. B. Shenoy, Topological Insulators in Amorphous Systems, Phys. Rev. Lett. **118**, 236402 (2017).

[25] I. Sahlberg, A. Weström, K. Pöyhönen, and T. Ojanen, Topological phase transitions in glassy quantum matter, Phys. Rev. Research **2**, 013053 (2020).

[26] Q. Marsal, D. Varjas, and A. G. Grushin, Topological Weaire-Thorpe models of amorphous matter, Proc. Natl. Acad. Sci. USA **117**, 30260 (2020).

[27] K. Pöyhönen, I. Sahlberg, A. Weström, and T. Ojanen, Amorphous topological superconductivity in a Shiba glass, Nat. Commun. **9**, 2103 (2018).

[28] H. Huang and F. Liu, Theory of spin Bott index for quantum spin Hall states in nonperiodic systems, Phys. Rev. B **98**, 125130 (2018).

[29] A. Agarwala, V. Juricic, and B. Roy, Higher-order topological insulators in amorphous solids, Phys. Rev. Research **2**, 012067(R) (2020).

[30] C. Bourne and E. Prodan, Non-commutative Chern numbers for generic aperiodic discrete systems, J. Phys. A: Math. Theor. **51**, 235202 (2018).

[31] Y. Barlas and E. Prodan, Topological classification table implemented with classical passive metamaterials, Phys. Rev. B **98**, 094310 (2018).

[32] M. N. Ivaki, I. Sahlberg, and T. Ojanen, Criticality in amorphous topological matter: Beyond the universal scaling paradigm, Phys. Rev. Research **2**, 043301 (2020).

[33] E. B. Sonin, Vortex oscillations and hydrodynamics of rotating superfluids, Rev. Mod. Phys. **59**, 87 (1987).

[34] D. Weaire and M. F. Thorpe, Electronic properties of an amorphous solid. I. A simple tight-binding theory, Phys. Rev. B **4**, 2508 (1971).

[35] D. P. Arovas, R. N. Bhatt, F. D. M. Haldane, P. B. Littlewood, and R. Rammal, Localization, Wave-Function Topology, and the Integer Quantized Hall Effect, Phys. Rev. Lett. **60**, 619 (1988).

[36] Y. Huo and R. N. Bhatt, Current Carrying States in the Lowest Landau Level, Phys. Rev. Lett. **68**, 1375 (1992).

[37] D. Leykam, A. Andreanov, and S. Flach, Artificial flat band systems: From lattice models to experiments, Adv. Phys. X **3**, 1473052 (2018).

[38] Unlike the previous argument, here we cannot prove a vanishing density of states, but for disordered or amorphous systems, the mobility gap is the physically relevant feature, given that the density of states need not vanish in the gap.

[39] P. W. Anderson, Absence of diffusion in certain random lattices, Phys. Rev. **109**, 1492 (1958).

[40] J. E. Avron, R. Seiler, and B. Simon, Homotopy and Quantization in Condensed Matter Physics, Phys. Rev. Lett. **51**, 51 (1983).

[41] A. Kitaev, Anyons in an exactly solved model and beyond, Ann. Phys. **321**, 2 (2006).

[42] R. Ma, C. Owens, A. LaChapelle, D. I. Schuster, and J. Simon, Hamiltonian tomography of photonic lattices, Phys. Rev. A **95**, 062120 (2017).

[43] T. A. Loring and M. B. Hastings, Disordered topological insulators via C*-algebras, Europhys. Lett. **92**, 67004 (2010).

[44] W. Kohn, Theory of the insulating state, Phys. Rev. **133**, A171 (1964).

[45] M. B. Hastings, Lieb-Schultz-Mattis in higher dimensions, Phys. Rev. B **69**, 104431 (2004).

[46] J. T. Chalker and P. D. Coddington, Percolation, quantum tunnelling and the integer Hall effect, J. Phys. C **21**, 2665 (1988).

[47] E. Abrahams, P. W. Anderson, D. C. Licciardello, and T. V. Ramakrishnan, Scaling Theory of Localization: Absence of Quantum Diffusion in Two Dimensions, Phys. Rev. Lett. **42**, 673 (1979).

[48] A. Lagendijk, B. van Tiggelen, and D. S. Wiersma, Fifty years of Anderson localization, Phys. Today **62**(8), 24 (2009).

[49] J. Li, R.-L. Chu, J. K. Jain, and S.-Q. Shen, Topological Anderson Insulator, Phys. Rev. Lett. **102**, 136806 (2009).

[50] Y. Xue and E. Prodan, Quantum criticality at the Chern-to-normal insulator transition, Phys. Rev. B **87**, 115141 (2013).

[51] C. W. Groth, M. Wimmer, A. R. Akhmerov, J. Tworzydło, and C. W. J. Beenakker, Theory of the Topological Anderson Insulator, Phys. Rev. Lett. **103**, 196805 (2009).

[52] S. Stützer, Y. Plotnik, Y. Lumer, P. Titum, N. H. Lindner, M. Segev, M. C. Rechtsman, and A. Szameit, Photonic topological Anderson insulators, Nature **560**, 461 (2018).

[53] E. J. Meier, F. A. An, A. Dauphin, M. Maffei, P. Massignan, T. L. Hughes, and B. Gadway, Observation of the topological Anderson insulator in disordered atomic wires, Science **362**, 929 (2018).

[54] I. C. Fulga, F. Hassler, A. R. Akhmerov, and C. W. J. Beenakker, Topological quantum number and critical exponent from conductance fluctuations at the quantum Hall plateau transition, Phys. Rev. B **84**, 245447 (2011).

[55] H.-H. Hung, A. Barr, E. Prodan, and G. A. Fiete, Disorder effects in correlated topological insulators, Phys. Rev. B **94**, 235132 (2016).

[56] C. Lanczos, An iteration method for the solution of the eigenvalue problem of linear differential and integral operators, J. Res. Natl. Bur. Stand. **45**, 255 (1950).

[57] I. U. Ojalvo and M. Newman, Vibration modes of large structures by an automatic matrix-reduction method, AIAA J. **8**, 1234 (1970).